ABSTRACT

Title of thesis: MORPHOLOGY EVOLUTION OF DROPLETS IN A POLYMER BASED EXTENSIONAL FLOW

Shri Harsha Bharadwaj
Master of Science, 2021

Thesis directed by: Professor David I. Bigio
Department of Mechanical Engineering

Fused Deposition Modelling (FDM) is one of the most widely used Additive Manufacturing (AM) methods to bring products to life. This thesis examines the incorporation of liquid additives into the nozzle region of an FDM system and attempts to understand their behavior in the polymer melt flow. The current computational work provides a background for a novel method wherein liquid additives can be injected into the melted polymer. A converging nozzle providing a near constant extension rate along the center-line is modelled. The deformation of droplets inside a polymer undergoing a purely extensional flow is studied for a range of exit (V) to platen velocities (U) and viscosity ratios (λ). It is observed that the behavior of droplets for a $\lambda = 1$ is found to be drastically different from that of lower λ's, which is attributed to the balance of shear stresses at the interface of the inner and outer flow fields. Finally, the morphology of the deposited plastic strands is also predicted. It is observed that as the velocity ratio (V/U) is increased the cross-section of the deposited strand changes from being almost spherical to an oblong.

MORPHOLOGY EVOLUTION OF DROPLETS IN A POLYMER BASED EXTENSIONAL FLOW

by

Shri Harsha Bharadwaj

Thesis submitted to the Faculty of the Graduate School of the
University of Maryland, College Park in partial fulfillment
of the requirements for the degree of
Master of Science
2021

Advisory Committee:
Professor David I. Bigio, Chair
Professor Dr. James Duncan
Assistant Professor Dr. Ryan Sochol

Dedication

This work is dedicated to my mother, uncles and my late grandparents. I would not be where I am today without their constant support and help. Thank you for standing by my side whatever the odds.

Acknowledgments

First and foremost I would like to thank my advisor, Professor David I. Bigio for giving me this wonderful opportunity to work on this project. It is said that the transition from an undergraduate to a graduate is difficult, but he made it easier for me with his expertise and knowledgeable conversations about the subject matter. I am extremely grateful for his constant guidance and encouragement. I would also like to thank Dr. James Duncan and Dr. Ryan Sochol for serving on my thesis committee.

I would like to acknowledge my colleagues at the Advanced Manufacturing Laboratory for their help during my tenure as a graduate student. Having learnt a great deal from Aditya Sangli, his research acted as an impetus for the current work and this work would not have been possible without his thoughtful recommendations. I would also like to thank Marcelo Arispe-Guzman for all his invaluable inputs throughout the years.

This work would not have been smooth if it were not for the constant support from my housemates. I would like to thank Rajath Dev and Shruthi Suresh for keeping me motivated and having my back, especially during the final stretch. I would also like to thank Harsha Naveendas and Haafiz Husker for their friendship.

Table of Contents

List of Tables

List of Figures

List of Abbreviations

ASTM	AMERICAN SOCIETY FOR TESTING and MATERIALS
AM	ADDITIVE MANUFACTURING
FFF	FUSED FILAMENT FABRICATION
FDM	FUSED DEPOSITION MODELING
CNC	COMPUTER NUMERIC CONTROL
DIW	DIRECT INK WRITING
SWNT	SINGLE WALLED CARBON NANOTUBES
PLA	POLYLACTIC ACID
ABS	ACRYOLONITRILE BUTADIENE STYRENE
PS	POLYSTYRENE
PET	POLYETHYLENE TEREPHTHALATE
HTPB	HIGH TEMPERATURE POLYMER BLENDS
HDPE	HIGH DENSITY POLYETHYLENE
PDMS	POLYDIMETHYLSILOXANE
LBADSA	LOW BOND AXISYMMMETRIC DROP SHAPE ANALYSIS
FVM	FINITE VOLUME METHOD
CAD	COMPUTER AIDED DESIGN
VOF	VOLUME OF FLUID
BOI	BODY OF INFLUENCE
SIMPLE	SEMI IMPLICIT METHOD FOR PRESSURE LINKED EQUATIONS

Chapter 1: Introduction

According to ASTM International, Additive Manufacturing (AM) which is more commonly referred to as "3D printing" is defined as a process in which objects are made by layered deposition of materials on top of each other, as opposed to subtractive manufacturing technologies [1]. Since its conception, AM technologies have grown to become widely popular and has changed the way in which many products are made and distributed [2]. AM technologies are being used in the medical industry in the form of bio-materials in order to manufacture orthopedic implants, bone grafts etc. They also have extensive uses in aerospace applications and in the field of architecture [3] [4].

1.1 Extrusion Based Additive Manufacturing

There are various types of extrusion-based processes. One among those is Fused Filament Fabrication (FFF) which is also widely known as Fused Deposition Modelling (FDM). Initially developed by Stratasys Inc, the process makes use of a thermoplastic material which is deposited on the build plate in succeeding layers.

The filament is drawn into the system from the spool with the help of feeding rollers and a stepper motor. The plastic gets melted as it passes through a heated

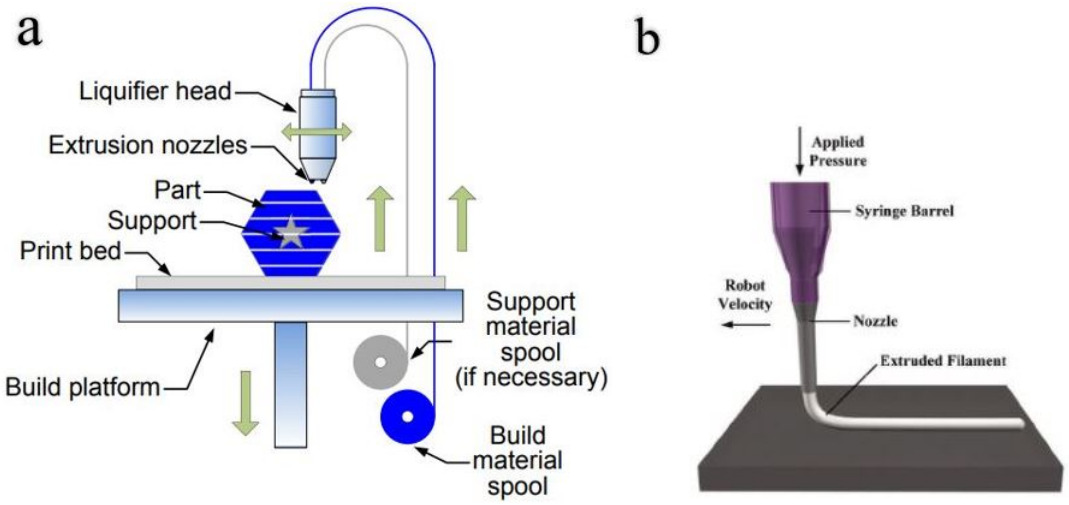

Figure 1.1: (a) A diagram of the FDM manufacturing process [5] (b) An illustration of continuous filament direct ink writing technique [6] [7].

liquefier which is heated well above the plastic's melting temperature. The resistor inserted into the liquefier is the source of heat. A thermocouple inserted into the block measures the temperature with the help of a feedback looping system. The melted polymer is forced out of the nozzle die of the printer. The movement of the printer head along the three Cartesian axes is made possible with the help of Computer Numeric Control (CNC). The operating temperature, extrusion rate, build orientation among others can be tuned to get the desired output.

Similar to FDM, in Direct Ink Writing (DIW) objects are created by controlled movements of the axes [6]. One of the main differences between the FDM and DIW is the usage of colloidal gels, nanoparticles or organic-based inks [6] instead of molten polymers. A hydrogel-based ink can also be used for DIW printing [8]. DIW which employs shear thinning gels are used in biomedical applications such as tissue engineering and drug delivery systems [9].

1.2 Composite Materials

Polymers when compared with ceramics and metals have inferior mechanical and thermal properties. Hence, depending on the application it becomes necessary to reinforce these polymer matrices with materials whose properties are orders of magnitude greater than that of the matrix [10].

A composite is a multi-phase material in which re-enforcing fillers are integrated with a polymer matrix, resulting in synergistic mechanical properties that cannot be achieved from either component alone [11]. For example, Single walled carbon nanotubes (SWNTs) are dispersed into commercial polymers in order to increase its electrical properties and applications without compromising the host polymer's processability and physical properties [12]. Emulsification is also a chief step in the manufacturing of medicinal tablets [13]. Colored dyes, stabilizers and anti-static agents are commonly added to polymers in order to enhance its properties [13].

The additive introduced into the polymer to improve specific properties are commonly referred to as "fillers". The polymer matrix acts as the continuous phase and the fillers act as discrete or continuous entities within the polymer phase [10]. However, most of the past research works deal with addition of solid filler [14] [15] into a molten filament. Hence, it is essential to understand the nature and effects of liquid fillers inside a polymer.

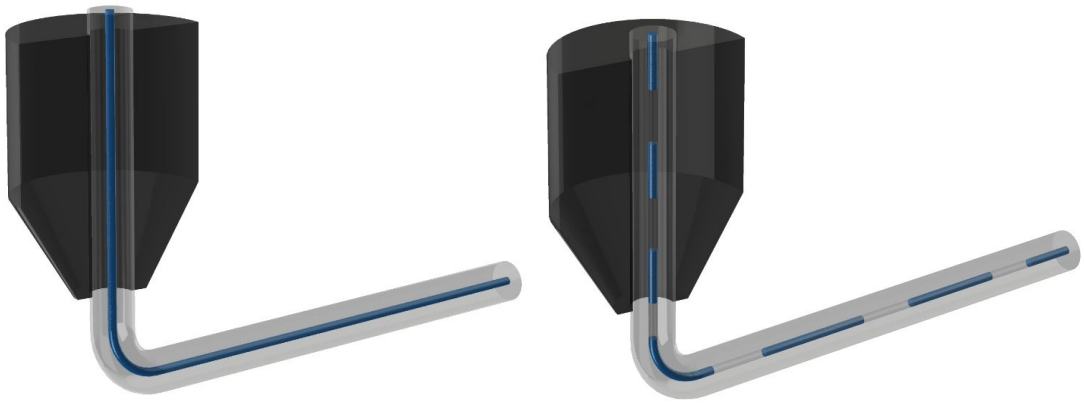

Figure 1.2: (a) Continuous reinforced composites are those which has a continuous flow of additive inside the polymer. The blue additive can be seen at the center, surrounded by the clear melted polymer from the extrusion nozzle, (b) Additives injected at discrete intervals of time are referred to as discontinuous reinforced composites.

1.3 Fundamentals of Droplet elongation and breakup

To create a polymer blend or an emulsion, a grasp of the size distribution of the droplet phase along with the understanding of the mean droplet size as a function of process conditions is essential to control the rheological and physical properties of the resultant product [13].

Certain forces play a vital role in understanding the behavior of the injected droplet into the system. Viscosity, interfacial tension and thereby the Capillary number are the three important factors that dictate the breakup and deformation of a droplet suspended in a polymer matrix.

G. I. Taylor [16] and S. Tomatika [17] proposed that in purely viscous Newtonian systems the deformation and breakup of droplets, in the absence of inertial forces is due to two dimensionless parameters [13]:

1. Viscosity ratio (λ): It is defined as the ratio of viscosity of the dispersed phase (η_d) to that of the continuous phase (η_c).

$$\lambda = \frac{\eta_d}{\eta_c} \tag{1.1}$$

2. Capillary number (Ca): Ca between two immiscible liquids is a quantity that relates the viscous and capillary forces. The viscous forces tend to elongate the droplets whereas the surface tension forces tend to make the droplet spherical [18]. The equation for the Capillary number is modified in order to take into account the droplet size and elongation.

$$Ca = \frac{b\dot{e}\mu}{\sigma} \tag{1.2}$$

where σ represents the interfacial tension between the two immiscible liquids (N/m), b is the unperturbed radius of the droplet (m), μ is the viscosity of the matrix or continuous phase (Pa-s) and $\dot{e}$ is the rate of deformation of the droplet (s^{-1}). There exists a Capillary number at which the droplet becomes unstable and breaks up into smaller droplets [13]. This is referred to as Critical Capillary number ($Ca_{critical}$). Changing the droplet size leads to change in the rate of deformation which in turn leads to change in Capillary numbers. Hence, it can be said that the transition from a stable drop to breakup is due to the imbalance in viscous and surface tension forces [19] [20].

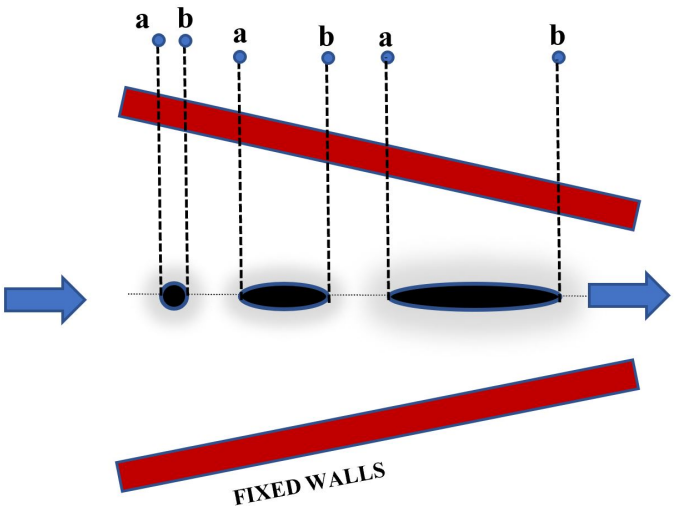

Figure 1.3: An illustration of elongational flow in a converging channel. As the drop stretches along the flow axis, its volume decreases in the perpendicular direction due to volume conservation.

1.4 Types of Flow fields

Rheology is the branch of physics that helps us understand how materials flow or deform under the application of forces. There are two types of deformational flows that are generally observed. In the simplest terms, extensional flow refers to those that have stretching along the streamlines in the principal direction of flow.

As seen in Fig.1.3 a particle defined by points a-b goes further apart as the deformation proceeds. This is also referred to as "irrotational flow" since the particles does not experience any rotation. In shear flow shown in Fig. 1.4 the particles not only elongates but also rotates.

Understanding the melt rheology of polymers and liquids in general forms the basis for manufacturing emulsions. While a liquid can be sheared indefinitely, extensional flow is a transient test as it is a function of time [21]. A fluid can only

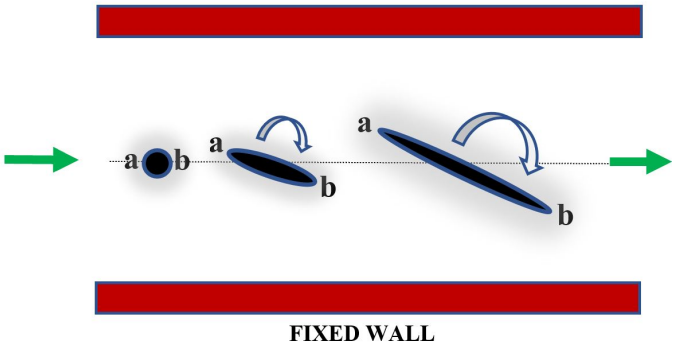

Figure 1.4: An artistic illustration of shear flow in a channel.

stretch to an extent, after which they become adequately thin and break up [21].

1.5 Applications

Understanding the behavior of droplets in converging channels provide us with a basis to manufacture polymers in the AM setup with several applications. Some of the applications are listed below.

(a) Fluid filled solid parts can be manufactured. This also gives way to manufacture products that have colored fillers inside clear filaments. With an efficient mechanism for controlled injection of the dye, both continuous and discontinuous reinforced composites can be manufactured.

(b) Based on the cross-section of the filament needed, different flow channels with novel cross-sections can be manufactured that might result in interesting morphologies of the droplets.

(d) Liquid additives having mechanical, thermal properties better than that of the existing filaments can be used in order to bring out the synergistic capabilities

between the two.

1.6 Objectives and Approach

Following in the footsteps of Sangli [22] this work aims to understand the behavior of droplets inside a melted polymer. Extensive work has been carried out with regards to addition of fillers into the raw plastic, thereby manufacturing polymer composites. The applications of these composites range from electrically conducting 3D-printed components [23] to bio ceramic fillers for biomedical applications [24]. These manufactured composites have better mechanical strength, durability and provides us with innumerable applications. Hence, development of novel kinds of composites by making use of the existing methodologies is necessary.

Among the different 3D printing processes, FDM is one of the most popular and commonly used. FDM due to its ease of accessibility coupled with availability and cost makes it the most ideal process for research purposes. In addition to the mentioned advantages, FDM also provides us with a range of plastics [Poly-Lactic Acid (PLA), Acrylonitrile Butadiene Styrene (ABS), Polystyrene (PS) and Polyethylene terephthalate (PET)] that have varying properties to work with.

A converging nozzle resembling an FDM nozzle is modelled. A droplet is suspended in the polymer. The nature of deformation of the droplets inside the polymer undergoing extensional flow is analyzed. Understanding the behavior of the additives forms a basis to 3D print novel composites using FDM technology.

1.7 Thesis organization

This thesis is divided into four chapters: Chapter 2 summarizes the research methodologies, theories and conclusions from past works. Droplet behaviors and experiments in various channels and the factors that are necessary to bring about extensional deformation in the droplets are discussed. Chapter 3 details the various numerical calculations necessary with regards to the rheology of the polymer and the droplet. It also illustrates the methodology used to perform the simulations. Chapter 4 discusses the results obtained. Chapter 5 discusses the future work that can be done with the current work as basis.

Chapter 2: Literature Review

2.1 Introduction to Polymer mixing

When two or more polymers are mixed together to create a state-of-the-art material with combined properties, it is referred to as polymer blending. These blends can either be miscible, partially miscible or immiscible. An immiscible blend is heterogeneous and there is a clear distinction between the different phases present in the system.

According to T. DeMeuse [25], High Temperature Polymer Blends (HTPBs) are categorized by their ability to withstand and perform their expected function at T $\geq$ 140$\hat{}\circ$C. They are particularly useful in the military and aerospace industries where they are needed for components experiencing high temperatures for long periods of time. Similarly, they are also used in electronic devices, batteries and can also be used as polymer electrolytes for super capacitors [26].

In any emulsion, the behavior of external fluid influences the flow of the internal fluid. When a drop is suspended in another fluid, the drop orients itself in the direction of the flow field. As discussed in Chapter. 1, λ between the two fluids play a vital role in determining the morphology. It has been observed that, λ between two polymer blends is a function of the molecular weights of the plastics as well as

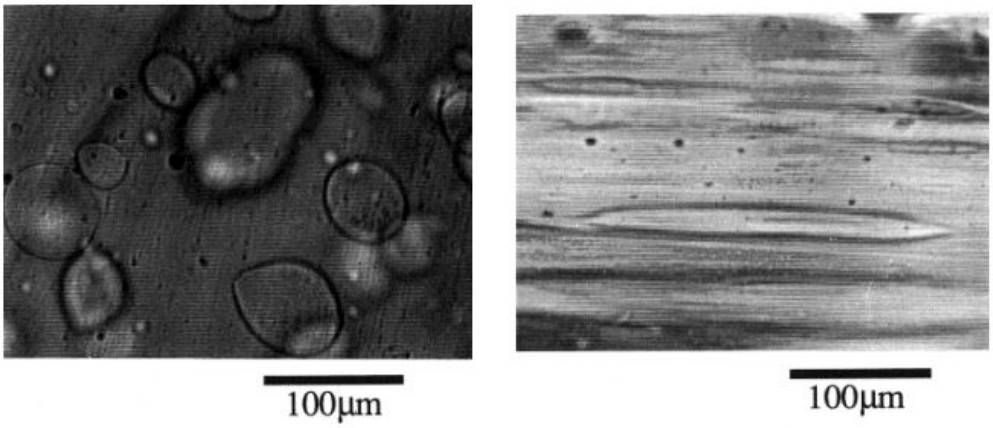

Figure 2.1: An immiscible polymer blend system of an Ultra-High-Molecular-Weight (UHMW) polymer and poly(Acryonitrile-co-Styrene) (AS) at 145°C when viewed through an optical microscope. Two stages: before (left) and after elongation (right) under a Hencky strain of 2.3 are shown [27].

the processing temperature of the melt [25].

It is imperative to have a look at past works that shine a light on the behavior of polymers and droplets subjected to varying boundary conditions.

2.2 Early Works

G.I. Taylor [28] in his pioneering work, explored the formation of emulsions by studying the deformation of the drop of one fluid by the viscous drag of the matrix fluid which surrounded it. The setup, shown in Figure. 2.11 consisted of four rotating cylinders mounted on the corners of a square. A hole was provided at the top to introduce a liquid. The two shafts rotated in opposite directions with the help of driving pulleys. This hyperbolically streamlined setup produced a planar extensional flow at the center of the channel. Documenting the droplet behavior, he came up with an expression given by

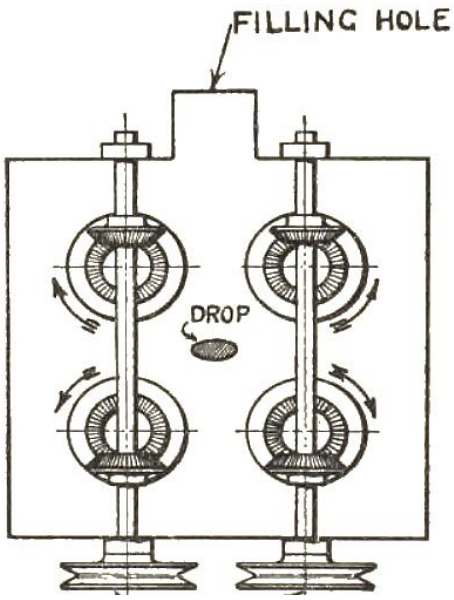

Figure 2.2: The device used by G. I. Taylor [28].

$$\frac{L-B}{L+B} = \frac{2C\mu a}{T}\left(\frac{19\lambda+16}{16\lambda+16}\right) \tag{2.1}$$

where L and B represent the length and width of the droplet. μ is the viscosity of the matrix fluid, a is the size of the droplet, T is the interfacial tension and C represents the strength of flow. The left hand side of the equation later came to be known as Taylor's deformation parameter (D). D = 0 for a sphere since L = B. His experimental observations were found to agree with Equation. 2.1, and he found that at lower λ's (0.0003), the droplet stretched indefinitely but did not break up. For small deformations, he came to the conclusion that the viscosity ratio of the fluids greatly affected the behavior of the droplet.

This major work formed a basis to study droplet behavior in channels having varying cross-sections. Since its conception, the four-roll mill has been widely used to study the droplet deformations [29], [30], orientation of polymer chains [31] and

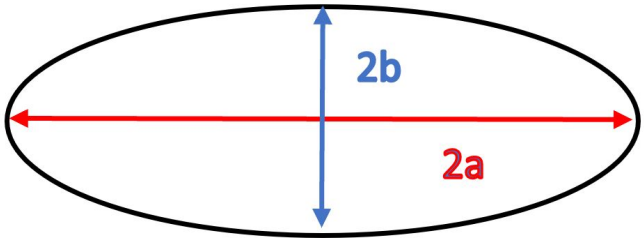

.

Figure 2.3: Illustration of axes of an ellipse. The ellipse represents a deformed droplet and references dimensionless D mentioned in Equation. 2.1.

even used in microfluidic devices to enhance mixing efficiency [32].

Lord Rayleigh [33] in 1879 examined the instability of jets and the transition of a long cylindrical incompressible viscous jets into smaller satellite droplets. He attributed this to the surface tension that worked against inertia. However, he neglected to consider the viscous effects of the surrounding medium. S. Tomatika [17] in 1935, considering both the surface tension and viscous effects investigated the instability of long cylindrical threads. He found that the maximum instability occurs at a definite value of the wavelength and this wavelength varies with λ, resulting in droplets of definite shapes.

Much later, transient behavior of droplets in different flow-fields were investigated in defining works of B.J. Bentley and L. G. Leal [34]. They studied the breakup of droplets for a wide range of viscosity ratios and provided the values for $Ca_{critical}$. For purely extensional flows Bentley et al. [34] reported that for a drop to break up, the critical Capillary number has to be in the range of $0.25 \geq Ca_{critical} \geq 0$. For flow fields wherein, an infinite amount of polymer is assumed to be flowing around a less viscous drop, the Ca will be extremely high and no bursting or breakup of droplets will be observed.

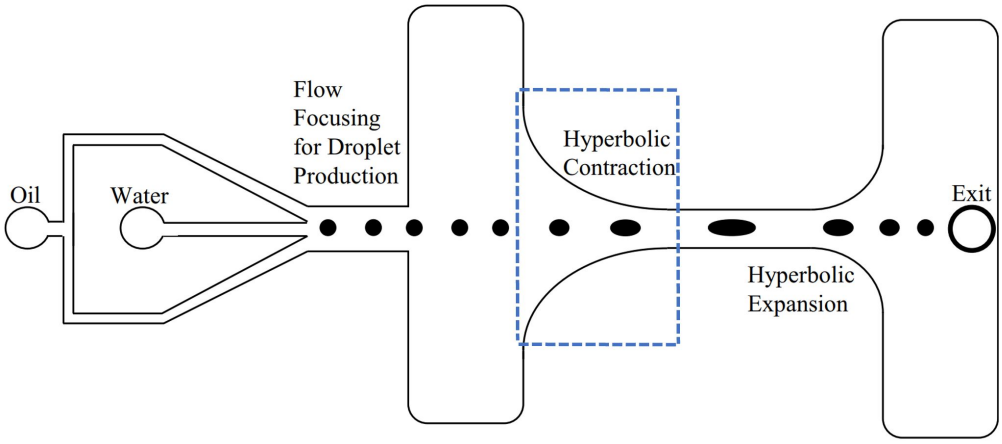

Figure 2.4: Flow cell used by Mulligan et al., fabricated using soft lithography techniques. The highlighted hyperbolic section was of interest in their experiments [19].

2.3 Droplet deformation in flow focusing devices

2.3.1 Hyperbolic Channels

The general principles and seminal works concerning droplet morphology were talked about in Section. 2.2. It is seen that cross-sectional areas of channels can be manipulated in order to study the changes in extensional effects [35]. This segment focuses on drop deformation in experimentally designed contractions.

Making use of microfluidics, Mulligan and Rothstein [19] developed a novel flow cell to understand the behavior of droplets in a hyperbolic contraction. The droplets were subjected to an uniform extensional flow and the effect of confinement-induced shear on droplet deformation and breakup were investigated. They defined confinement as

$$C = \frac{R}{w_2} \tag{2.2}$$

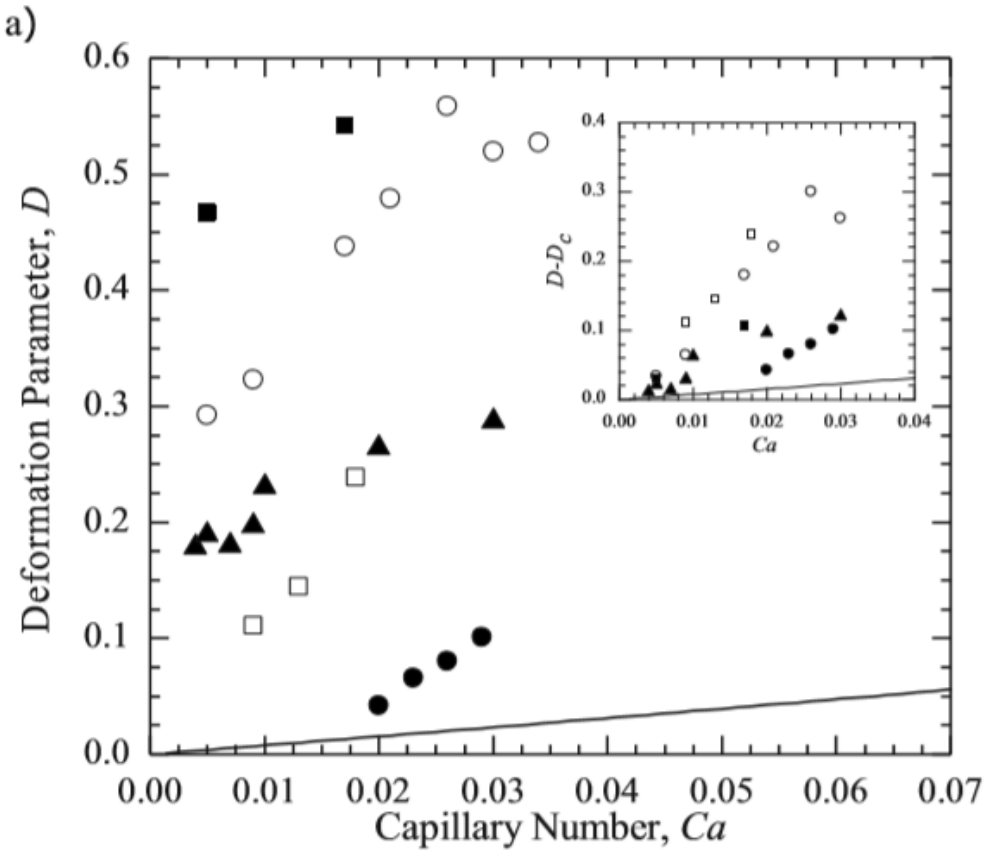

Figure 2.5: Graph showing Deformation parameter (D) as a function of Capillary number for water drops in oil. Confinement parameters corresponding to the different shapes are 0.66, 0.99, 1.3. 1.5 and 2.0 from bottom to top [19].

where R is the initial radius of the droplet and w_2 is the half width of the gap the drop was confined in. As is the case with any channel, the shear effects are maximum at the walls and as we move towards the center-line, the shear rate becomes zero. One of the important reasons to study droplet behavior in microfluidic channels is the fact that they give rise to considerably higher extension rates [35]. With this setup, Mulligan et al., [19] had a range of $37\text{s}^{-1} < \dot{\epsilon} < 2100\text{s}^{-1}$.

They observed that increasing the confinement led to increase in the deformation of droplets regardless of the Capillary numbers. They deduced that an unconfined droplet will always elongate less than that of drop having higher con-

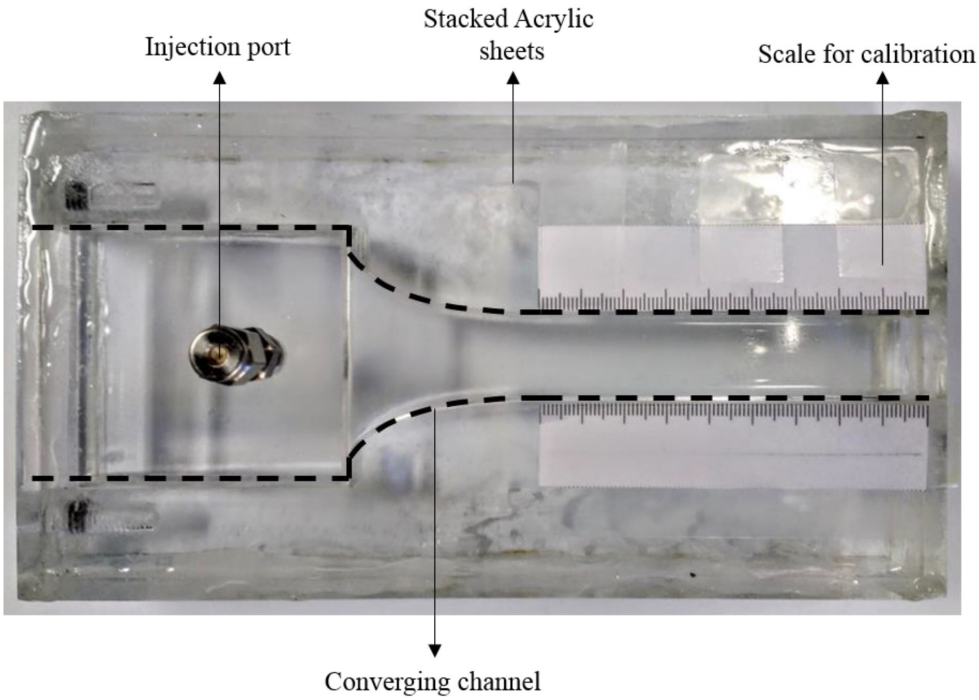

Figure 2.6: Hyperbolic channel having a rectangular cross-section made out of Plexiglas used in Sangli's [36] experiments.

finements. This was evident in our simulations when increasing the diameter of the nozzle gave rise to droplets having less elongation in the axial direction.

Most of the commonly used setups to study the behavior of droplets are extremely difficult to be adopted into a manufacturing setup. Using Mulligan's [19] microfluidic channel as a reference, Sangli [36] designed a macro-scale hyperbolic setup and investigated the deformation and breakup of Castor oil droplets in a silicone oil matrix.

Sangli observed that the Capillary numbers decreased as the droplets traversed the channel and droplets having higher Capillary numbers elongated faster than the ones with lower initial Capillary numbers. It was also evident from his work that droplets injected at offset positions elongated more due to the effect of shear than

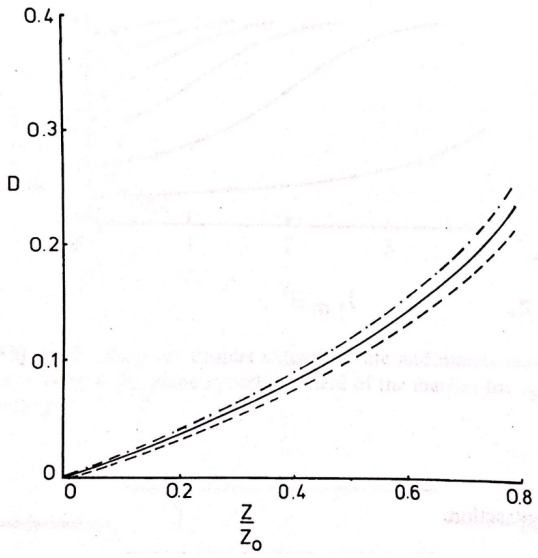

Figure 2.7: The upper most, middle and lower curve represent interfacial tensions of 2.5 x 10^{-3} N/m, 5 x 10^{-3} N/m and 10^{-2} N/m respectively for $\lambda = 10$.

the ones deployed at the center-line. This was attributed to the velocity gradient being an order of magnitude higher in offset positions. While the center-line droplets underwent symmetrical deformation about the axial direction, there was evidence of asymmetry for drops undergoing both elongation and shear. There was also evidence of rapid width reduction at the leading end of the droplets. This work was a stepping stone to pave way to additive manufacturing dies where unique morphologies of liquid droplets could be observed inside an exterior solid filament.

2.3.2 Conical Channels

Most of the elongational flows seen in practical applications, especially in polymer processing, involve axisymmetric contractions as opposed to hyperbolic contractions. Among others, one of the main reasons for this is the difficulty to manufacture hyperbolic dyes using traditional machining practices. Hence, extensional flows in

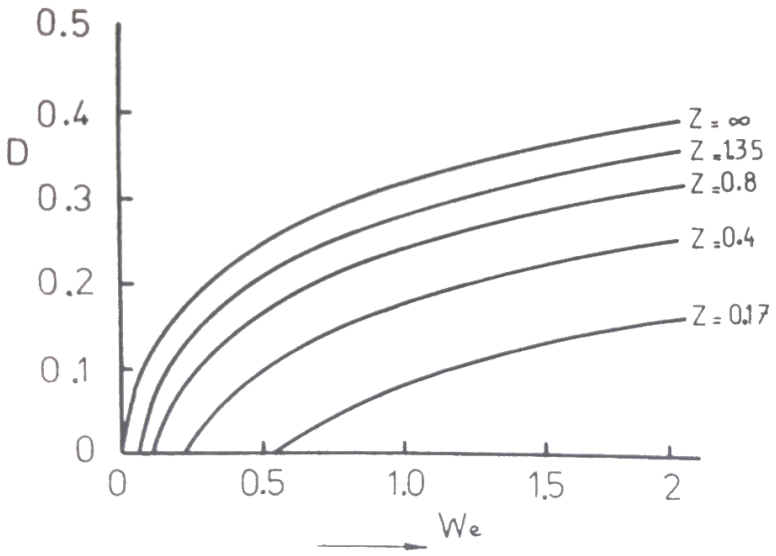

Figure 2.8: Variation of droplet behavior with Capillary number as a function of cone length (Z) [37]. Cone length is defined as the total length of the converging channel.

axi-symmetric channels have to be looked into.

The dependence of interfacial tension on the deformation of droplets at high viscosity ratios was studied by Van der Reyden et al., [37]. Deformations in conical contractions was of primary interest in their work. Due to decreasing contraction, the deformation was not found to be constant which in turn increased the elongation. They stated that at high viscosity ratios, the interfacial effects had no dominance and the droplet deformation was independent of interfacial tension. Fig. 2.7 shows the change in deformation parameter at various positions in the conical channel. It is evident that even with significant variation in the interfacial tensions, there is not much difference in the deformation of the droplet. Rauwendall [37], thus concluded that for manufacture of emulsions having high viscosity ratios, elongational flows are more effective than shear flows.

Han et al., [38] studied the extensional deformation of a viscoelastic droplet

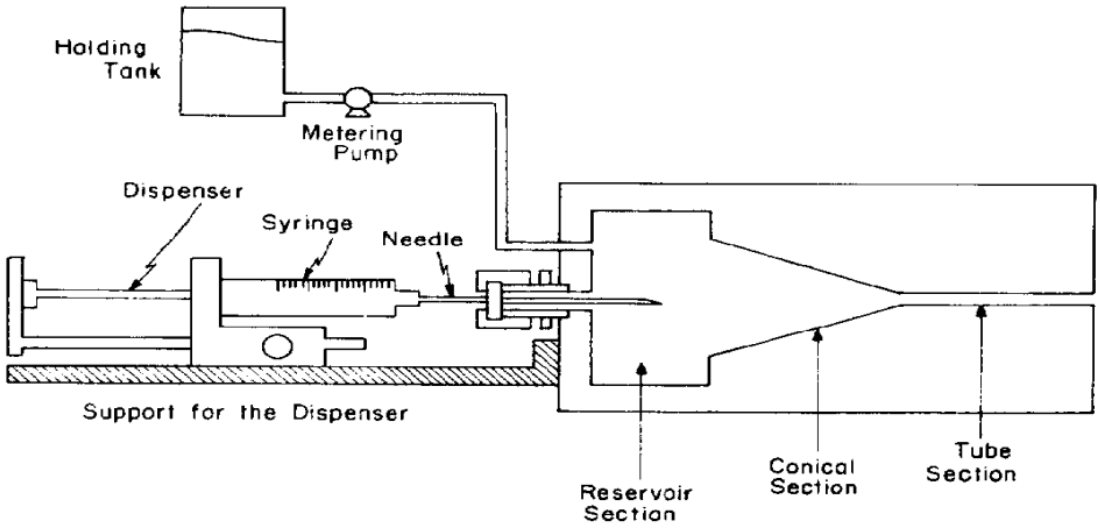

Figure 2.9: Experimental test rig built by Han et al., [38].

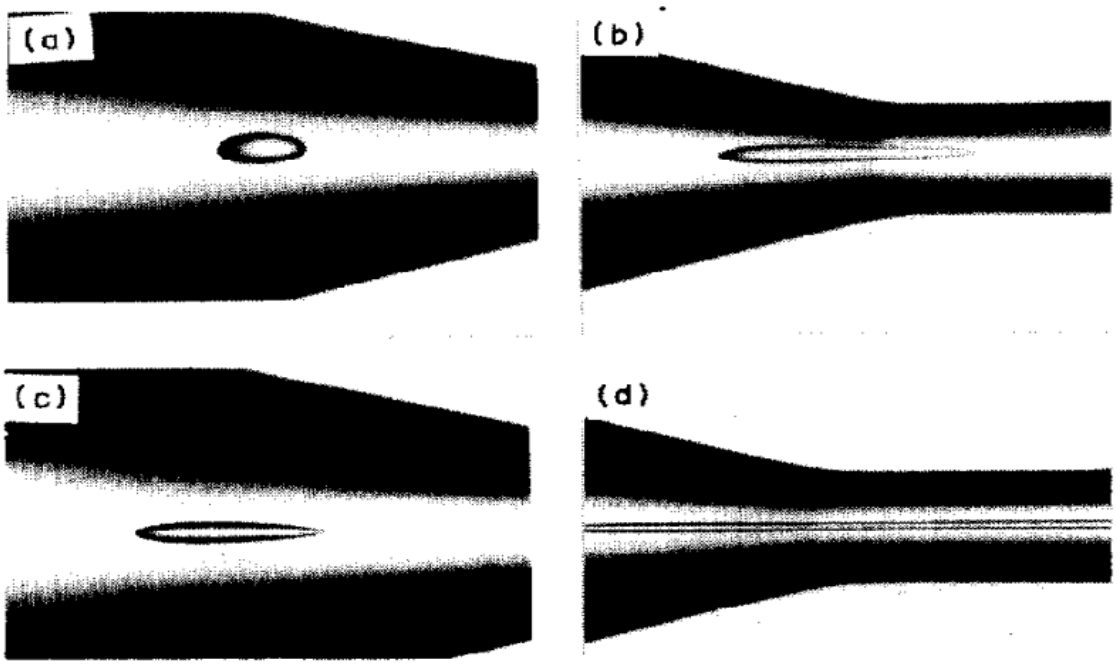

Figure 2.10: Images illustrating the evolution of droplet morphology through the channel for two different shear rates: (a) and (b) at = 13.7 s^{-1} , (c) and (d) at 128.7 s^{-1} [38]. The initial diameter of the droplet is D˙o = 1.20mm.

suspended in a viscoelastic medium. An experimental setup consisting of a dispensing system and a converging channel as seen in Fig. 2.10, was built. The setup was modelled such that the tube section provided Poiseuille flow and the conical section provided purely extensional flow along the center-line. The effect of shear rate and droplet size were documented. It was seen that a droplet subjected to a higher shear rate experienced the highest deformation. In the entrance region of the conical section, a steady state extension is seen. However, as the gradient in the convergence decreases, the velocity increases swiftly and an unsteady extensional flow is observed. It was also seen that droplets suspended in a medium having a higher viscosity deformed more. Hence, a decrease in the viscosity ratio yields a higher D.

2.4 Shear thinning of plastics

Most fluids that we see exhibit non-Newtonian behavior. Hence, their viscosities are dependant on shear rates. Shear-thinning fluids are those who's viscosity decreases with increase in shear rate. Pseudoplastics are commonly defined by two material specific parameters: consistency index and flow behavior index. Using a rheometer, the values of K and n can be obtained by measuring the fluid viscosity with different shear rates. In shear-thinning regimes, Ostwald-de Waele relationship also referred to as Power Law model can be used to establish the relationship

between the viscosity and shear rate of the fluid.

$$\tau = K * (\dot{\gamma}^n) \tag{2.3}$$

$$\nu = K * (\dot{\gamma}^{n-1}) \tag{2.4}$$

where τ is the shear stress, ν is the apparent viscosity (Pa-s), K is the consistency index (Pa-s^n), γ is the shear-rate (s^{-1}) and n is the flow behavior index (dimensionless). For a shear-thinning fluid n is always between 0 and 1.

In extensionally dominated flows, it becomes imperative to measure extensional viscosity as the fluid passes through the contraction. Cogswell [39], in 1978 while profiling flows in different cross-sections, proposed a way of measuring extensional viscosity by measurement of pressure drop along the channel. For an unlubricated constrained convergence, stretch rate is maximum along the centerline and he proposed an updated expression from his own previous work [40]. The expression that related the stretch rate to the cone half-angle (θ) and power law index (n) was given by,

$$\dot{\epsilon}_{max} = \left(\frac{3n+1}{n+1}\right)\frac{\dot{\gamma}}{2} tan\theta \tag{2.5}$$

Despite evidence [42] regarding the shear thinning behavior of polymer flows, no quantitative evidence existed to definitely say that the flows through converging nozzles were stretching flows. Drexler et al., [39] [43] looking into velocity gradients in a molten polymer flow conclusively proved the nature of extensional stretching in

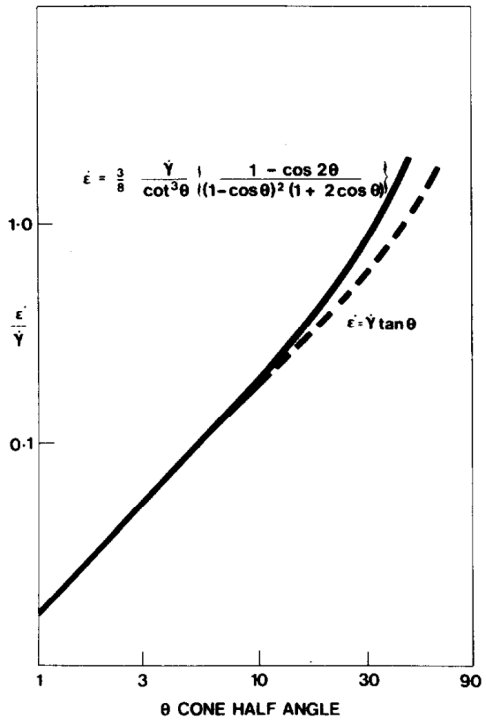

Figure 2.11: Graph illustrating maximum stretching for a Newtonian fluid under constrained convergence. The curves given by Cogswell [39] and Harrison [41] are compared.

converging dyes.

2.5 Droplet deformation in polymer blends

Viscoelasticity of the polymer melts makes it more difficult to understand the process of droplet deformation and breakup. The below mentioned works dictate as to how the behavior of melted polymer affects the morphology of the droplets suspended in it.

Muller et al., [44] [45] designed an experiment to determine the transient deformation of droplets in an extensional flow. This method made it possible to analyze polymer melts whose glass transition temperature was greater than that

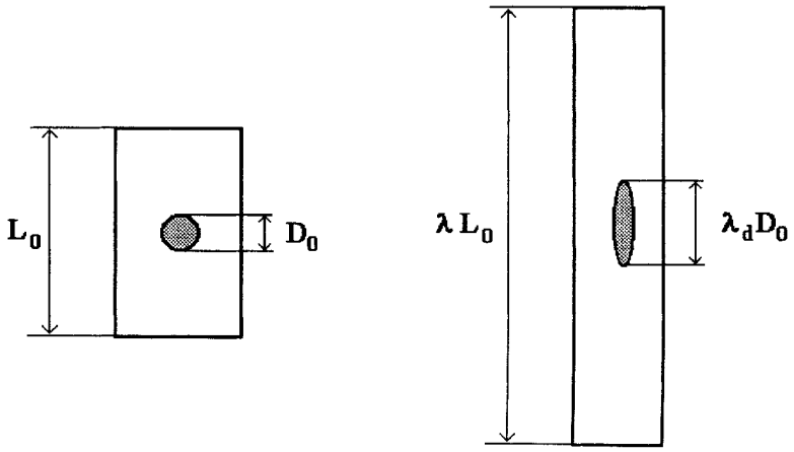

Figure 2.12: An illustration of a drop inside a polymer before and after deformation. The Cauchy deformation of the droplet is defined as the ratio of length of the elongated droplet ($\lambda_d D_o$) to the initial unperturbed droplet diameter D_o.

of the room temperature. A small number of spherical inclusions of High Density Poly-Ethylene (HDPE) were placed on the surface of the pure and clear polystyrene (PS). Another layer of the matrix polymer was placed on top of this setup and molded together at 180°C. These samples were then heated and stretched at a constant strain rate $\dot{\epsilon}$. Once the prescribed deformation was reached, the sample was immediately quenched in cold water to freeze the deformation of the droplet. Microscopic observations were later made to tabulate the findings. They report that since the specimens were quenched almost immediately after elongation, no interfacial instabilities were observed.

Based on Taylor's [28] [46] [44] theory, at high Capillary number flows, the contribution of interfacial tension can be neglected. Hence, the Cauchy deformation of the droplet and the matrix phase is given by

$$\frac{\lambda_d - 1}{\lambda - 1} = \frac{5}{2p + 3} \tag{2.6}$$

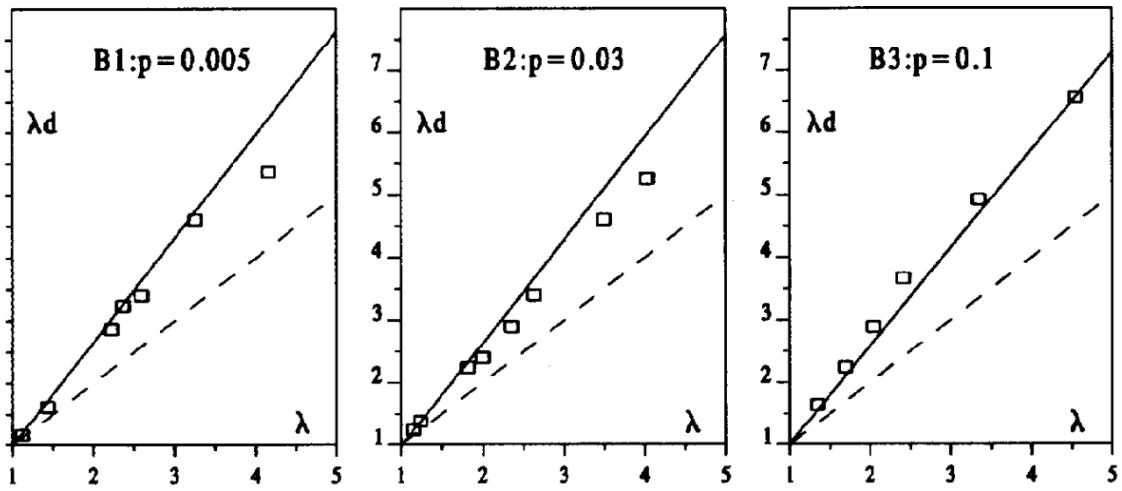

Figure 2.13: Graphs showing the relationship between the deformation of the matrix and the droplet phase for different polymer blends. The bold, squares and dotted lines represent the curves generated using Equation.2.6, experimental data and when $\lambda_d = \lambda$.

where p is the viscosity ratio between the phases, λ_d and λ are the droplet deformation and macroscopic deformation of the matrix.

It was observed that when different blends of the polymers were subjected to a constant $\dot{\epsilon}$ of 10^{-2} s^{-1}, for λ upto 3, there was a linear increase in the deformation between the two phases. Corroborating his experimental results with Equation. 2.6, Muller [44] [45], concluded that regardless of blends, when the viscosity of the drop is higher, it deforms less than that of the surrounding matrix phase. Whereas, when the viscosity of drop is less, the drop deforms more than the matrix medium. For values of p's greater than 1, the left-hand side of Equation. 2.6, tends to zero. Muller [45], also gave a limiting factor of 1.7 for $\frac{\lambda_d - 1}{\lambda - 1}$ as p $\rightarrow$ 0.

Although, Equation. 2.6 is only applicable to small deformations, it is found that the simulation and experimental results seemed to agree for large deformations upto $\lambda = 5$. As Migler et al., [18] puts it, there are two main disadvantages with

this process: it only samples a limited number of materials and even though Muller et al., [44] reports that quenching is done almost immediately after elongation, there still might be changes occuring in a fraction of second before the samples are quenched. Hence, this might not be an accurate representation of the behavior of the droplets.

Varanasi et al., [13], investigated the breakup of both purely Newtonian and viscoelastic droplets suspended in a Newtonian matrix. Using a transparent counter rotating cone and plate rheometer, he subjected various combinations of droplet and matrix phases to a simple shear flow.

The largest diameter droplet at the periphery of the rheometer was identified for a given shear-rate, after which shearing was brought to rest. The shear-rate was once again brought back to its original value in successive increments to monitor the droplet deformation for each step increase in shear-rate. When, the shear-rate was increased beyond a certain value ($\gamma_{critical}$), the already deformed threadlike droplets ruptured into smaller droplets. Hence, the maximum diameter of a droplet and $Ca_{critical}$ that could be produced at any shear-rate could be tabulated.

Using normal stress difference, corresponding to the shear-rate in the continuous phase at which the drops broke up, they evaluated elasticity of the droplets. It was found that the $Ca_{critical}$ for viscoelastic drops not only depended on the $\gamma_{critical}$, but also on the elasticity of the droplet. They proposed the existence of a shear-rate γ^*, which decreased with decrease in the elasticity of the droplet. They observed that not only were the viscoelastic droplets easier to breakup but also gave smaller daughter droplets when compared to Newtonian droplets, which was attributed to

the presence of high tensile stresses for viscoelastic drops.

According to Tavgav [47] [13], the elasticity of the matrix phase plays a vital role in the deformation of the dispersed droplets. For low viscosity ratios it was seen that the elasticity of the matrix phase stabilized the droplet and for high viscosity ratios, it destabilized the droplets.

Works of Migler et al,. [18] [48], shine a light on the drop deformations in polymer blends in channel flows. While studying the deformations of polystyrene drops in a polyethylene matrix they found that the droplets transitioned from ellipse to a string and back to a sphere in an optical slit die. This was accounted to the viscoelasticity of the drop. Migler [48], in one of his other works also proclaimed that in a viscoelastic medium, the droplets have the tendency to align themselves in the direction of vorticity. Gauthier et al,. [49] said that there was no difference in the behavior of viscoelastic and Newtonian droplets for very low viscosity ratios.

Even though the past works describe the behavior of droplets in various flow-fields and conditions, none of them explore the effect of the matrix flow-field on the drop once the drop has left the channel and is under continued shear. This work does precisely just that and provides a way for such a setup to be incorporated into a manufacturing process.

Chapter 3: Rheological Measurements and Model Setup

3.1 Design of the nozzle

Commercially available 3D printer nozzles have diameters ranging from 0.3 to 0.75mm. Nozzles having diameter greater than 0.75mm are used for custom print-jobs. These nozzles have the capability of accommodating less volumes of the melted filament. As seen in Figure. 3.1, the length of the conical section in a commercially available nozzle is approximately 1.4mm.

Adopting Sangli's [22], scaling of 1:10 for the drop size to outlet diameter of the nozzle, the currently available nozzles make it very difficult to inject a droplet 1/10th the size of the nozzle diameter. With these dimensions it is practically very difficult to perform droplet injection experiments. Hence, a modified nozzle that could be feasible to implement into a manufacturing setup has to be designed.

In order to inject a sufficiently large enough drop and study the nature of extensional flow, a nozzle having a higher diameter is modelled. Not only does this decrease the pressure drop significantly, increasing the length and gradient of conical section results in higher strain-rates amounting to a higher degree of deformations.

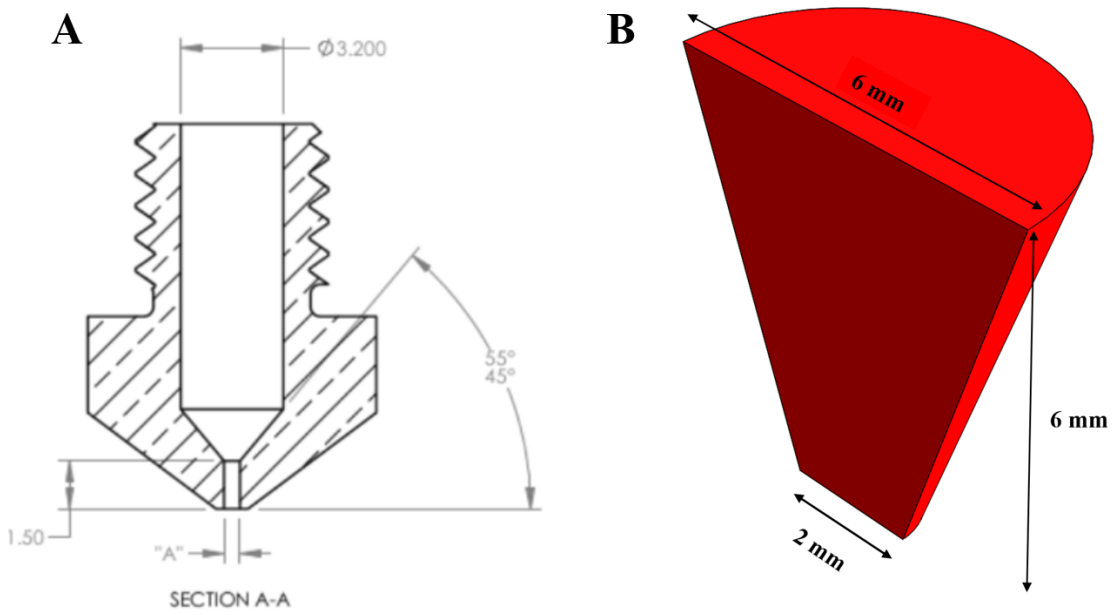

Figure 3.1: (A) Drawing of a commercially available Lulzbot TAZ4 nozzle. (B) Illustration of the design and dimensions of the nozzle used for this study.

3.2 Materials

A blend system is modelled wherein, silicone oil (Polydimethylsiloxane - PDMS) droplets could be injected into a viscous polymer flow. The melted polymer acts as the matrix phase and the silicone oil acts as the additive or droplet phase. Silicone oil is chosen as the additive for reasons mentioned below.

(a) Since the real-life 3D printing process is performed at high temperatures, the additive selected should have a high enough boiling and flash point. They are found to be >315°C and >295°C respectively for Silicone oil.

(b) Silicone oil has been the choice of fluid for some of the pioneering works [28] [34] investigating droplet dynamics and is available in a wide range of viscosities.

3.3 Interfacial Tension measurements

Interfacial tension exists between the interface of a liquid phase of a substance and the solid phase with which it is interacting. It is a measure of force of attraction between the molecules at the interface of the two substances in play [50]. As discussed in Chapter 1, in order to accurately predict the behavior of the droplets, it is important to know the interfacial tension between the two fluids. However, the interfacial tension between silicone oil and PLA is not reported in literature. Hence, it becomes necessary to employ methods that will aid us in determining the interfacial tension.

Sessile or pendant drop technique is widely used to determine the contact angle between the two surfaces. The drop who's contact angle is to be measured is deposited on a surface and measurements of the enlarged drop (radius, maximum height) are taken. However, this manual method of measurement is prone to errors, especially if the drop is hydrophobic. Hence, to validate the results obtained from the Sessile drop method, an alternate method of determining the surface tension is employed.

3.3.1 Sessile Drop Technique

When deposited on a smooth surface, the contact angle of a drop is independant of the drop size. A smooth textured black PLA sheet of 0.060" thickness and 1"x 1" dimensions is placed on a flat surface. A silicone oil drop of controlled volume using Hamilton^{TM} precision syringe is deposited on the plate. A measurement scale

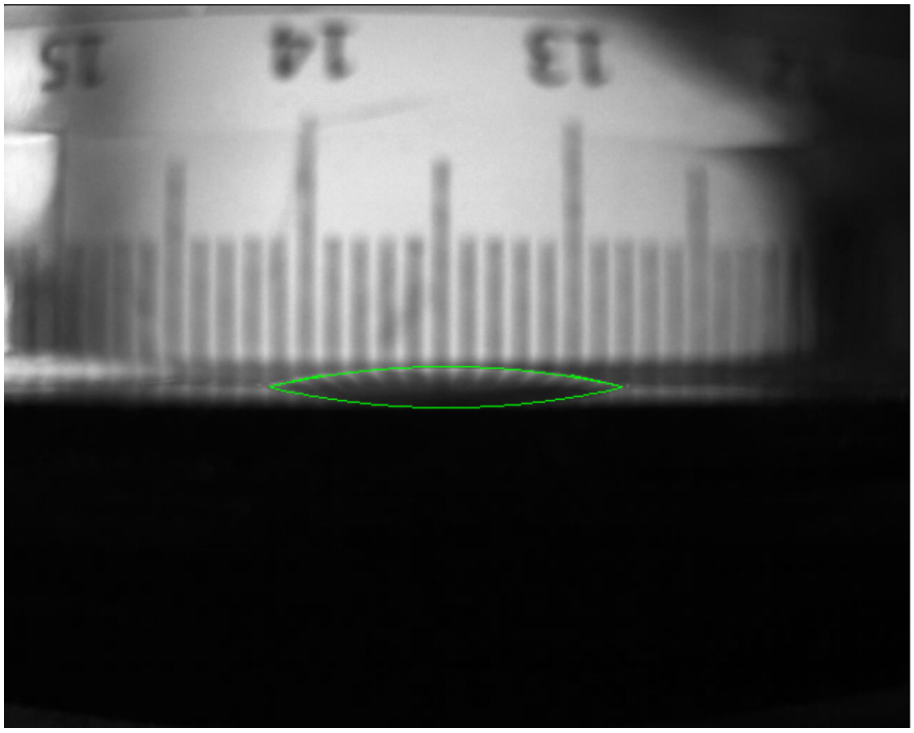

Figure 3.2: Captured image of the drop is converted to greyscale in order to measure the contact angle. The volume of the drop deposited is 0.01mL.

is fixed in the background in order accurately quantify the height and diameter of the droplet. A camera developed by FLIR Systems^{TM} called Chameleon3 is used to capture the images. Different volumes of drops are deposited and multiple trials are taken in order to make sure the calculated contact angle is as accurate as possible. Low-Bond Axisymmetric Drop Shape Analysis (LBADSA) [51] plugin available on Image-J, developed by EPFL is used for the measurement of contact angle.

German physicist Georg Hermann Quincke in 1870 derived an equation that related the surface tension to the contact angle of the drop [52] [53]. The Quincke relationship is given by

$$\sigma = \frac{\rho g h^2}{2(1 + Cos\theta)} \tag{3.1}$$

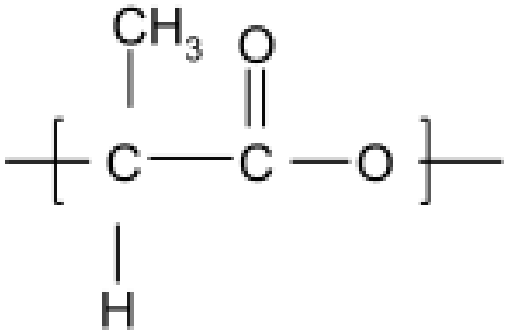

Figure 3.3: Chemical Structure of Poly-Lactic Acid [57]

where σ is the interfacial tension (N/m), ρ is the density of the drop, g is the acceleration due to gravity, h is the maximum height of the deformed droplet and θ is the contact angle.

Behroozi [54] noted that equation 3.1 was only exact for infinitely large drops where the surface curvature is mostly along the vertical plane, as this expression does not take into account the curvature of the drop along the horizontal plane. He calculated the error for smaller drops for be approximately 5%. The errors during the measurement coupled with inherent errors with Quincke's relationship, adds a lot of uncertainty for the measured values.

3.3.2 By method of Parachor

Parachor is widely used in organic chemistry to calculate the interfacial tension between two substances. One among its many applications is its usage in determining interfacial tensions between oil/gas [55]. Parachor is an additive quantity which relates the surface tension to the chemical structure [56]. The molar parachor is an empirical constant for a particular substance and is defined as

Unit	Parachor
O	20.0
C	4.8
H	17.1
Double bond	23.2

Table 3.1: Sugden's parachors for organic compounds [61].

$$P_s = \frac{(\gamma)^{0.25} M}{\rho} = (\gamma)^{0.25} V \tag{3.2}$$

where P_s is the Parachor, γ is the interfacial tension between the substances, M and ρ are the molar mass and density respectively. Surface tension of solid polymers can then be calculated using

$$\gamma = \left(\frac{P_s}{V} \right)^4 \tag{3.3}$$

Using the above expression the surface tension of PLA is found to be 38.58 mJ/m^2 which is in agreement with the experimentally calculated values for PLA [58], [59], [60].

Although, there existed models proposed by various authors, best consolidated by Van Oss et al., [62] most of them were accurate to a varying degree and there were vast differences between the experimentally and numerically calculated values of interfacial tension. Girifalco and Good [63] in 1957 proposed an equation to determine the interfacial energy between a solid and a liquid. In order to account for the variation between the values, they introduced an interaction parameter (ϕ). The equation is given by

	Volume (cm^3)	**Measured Height** (cm)	**Contact Angle** (θ)
Trial 1	0.01	0.04	13°
Trial 2	0.015	0.04	13°
Trial 3	0.02	0.04	13°

Table 3.2: Drop measurements

$$\gamma_{sl} = \gamma_s + \gamma_l - 2 * \phi * (\gamma_s \gamma_l)^{1/2} \tag{3.4}$$

where γ_{sl} is the interfacial energy, γ_s, γ_l are the surface energies of the solid and liquid phase respectively. The interaction parameter(ϕ) is defined as,

$$\phi = \frac{4(V_s * V_l)^{1/3}}{(V_s^{1/3} + V_l^{1/3})^2} \tag{3.5}$$

where V_s and V_l are the molar volumes of the solid and liquid respectively.

Considering a liquid and a solid system, Young's equation relating the surface energies and the contact angle is given by,

$$\gamma_{sl} - \gamma_s + \gamma_l cos\theta \tag{3.6}$$

Equating 3.4 and 3.6 we can eliminate γ_{sl} to get,

$$\gamma_s = \gamma_l \frac{(1 + Cos\theta)^2}{4\phi^2} \tag{3.7}$$

Hence, with the contact angle known, we can determine the value of γ_l. The values obtained for interfacial tension is tabulated in table 3.3. As expected there is

Contact Angle (θ)	**Quincke's Method(mJ/m^2)**	**Using Parachor(mJ/m^2)**
13°	29.73	38.58
13.341°	34.17	38.61
13.323°	35.20	38.61

Table 3.3: Interfacial Tension values obtained by using two different methods

no clear pattern of interfacial tension values from the Quincke's method due to error in measurements. Since parachor method is found to be more accurate, a value of 38.58 (mJ/m^2) is used as the interfacial tension.

3.4 Model Introduction

Multiphase simulations were performed using ANSYS Fluent, Academic Research, Release 20.2. ANSYS Fluent^{TM}, based on Finite Volume Method (FVM) numerically solves a set of mathematical equations to check for conservation of mass, momentum, species etc. among others. The equations that best describe an incompressible flow is given by the Navier Stokes equations.

$$\nabla \cdot u = 0 \tag{3.8}$$

$$\rho \frac{\partial \vec{u}}{\partial t} = -\nabla p + \mu \nabla^2 \vec{u} + \rho \vec{g} \tag{3.9}$$

where 3.8 and 3.9 represent continuity and momentum conservation, u represents the velocity vector flow field, g is the body acceleration, p is the pressure, ρ and μ are the density and viscosity of the fluid respectively.

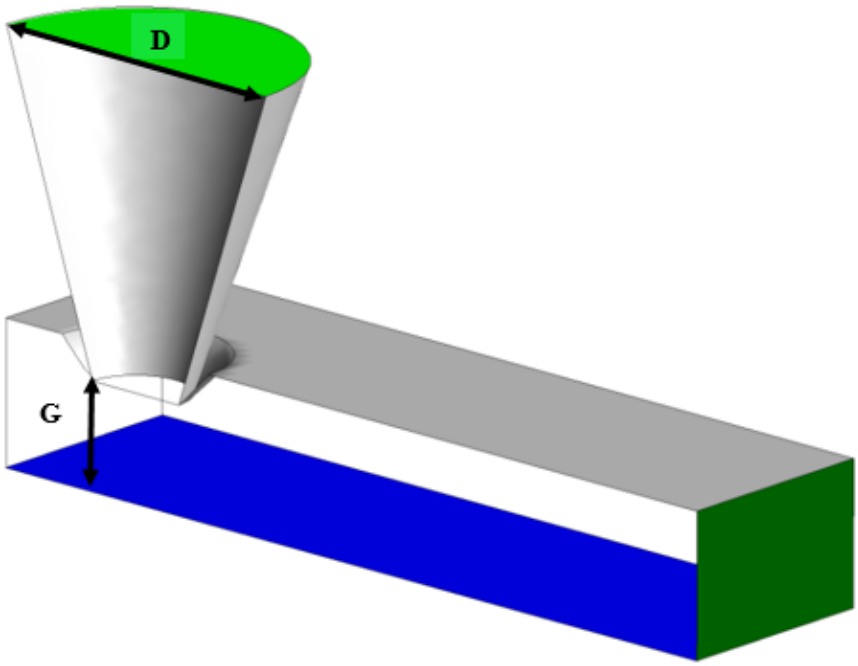

Figure 3.4: The designed geometry using SolidWorks. The diameter of the nozzle (D) and the gap distance between the nozzle outlet and the build plate (G) is highlighted.

A CAD model simulating the flow of plastic in a converging dye used in a FDM setup is designed using SolidWorks^{TM} 2020. As with any Computational Fluid Dynamics simulation the designed model is initially discretized after which boundary conditions are setup. Choosing the appropriate solver, the deposition of a defined length of strand on a moving build plate is emulated under varying conditions. The change in morphology of the plastic and the drop is predicted.

3.5 Model Description

Comminal et al. [64] simulated the effects of deposition flow of a molten plastic through the nozzle. He considered two dimensionless parameters to investigate its effects on the cross section of the strand. He characterized them as the velocity

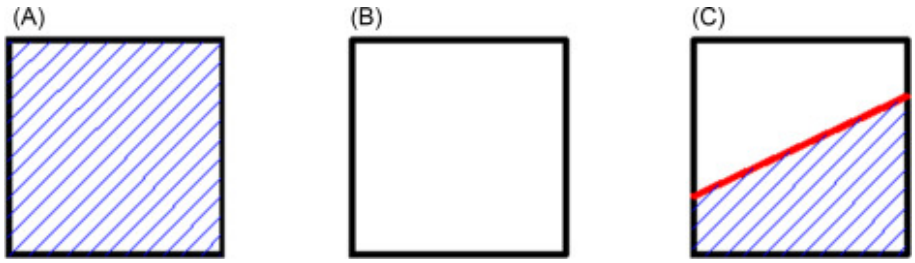

Figure 3.5: The fraction of a fluid present in a control volume: $\phi = 1$, 0 and 0.5 respectively. A volume fraction of 0.5 represents the interface line between two phases. [65].

ratio (V/U) and the normalized gap (g/D). However, the model assumed that the nozzle geometry to be cylindrical for simplification purposes. A constant cross-section cylindrical channel does not impose extension on droplets. Hence, in order to accurately model the real-life FDM setup, a design emulating flow on a plate as seen in Figure. 3.4 is used. The droplet enters a 3:1 axisymmetric contraction. The considerations made regarding the flow are summarized below.

(a) The inertial forces are very small compared to the viscous forces. Hence we have Stokes flow where $Re \ll 1$. Hence the flow inside the nozzle is a low Reynold's number, incompressible flow.

(b) In the real-life FDM printing process, there exists a temperature gradient from the nozzle to the heating block, which might lead to contraction or expansion of the filament post deposition. However, the effect of temperature is not accounted for in the current work.

(c) Since the inlet is oriented in the negative Z direction, gravity is accounted for. Although, it is found that its effect on the flow is negligible.

(d) During the operation of an FDM printer, the printer head containing the nozzle

moves while the build plate is fixed. It is extremely difficult to model such a setup. However, we can say that the motion of the build plate and the nozzle are relative to each other. Hence, the current model simulates the opposite configuration [64].

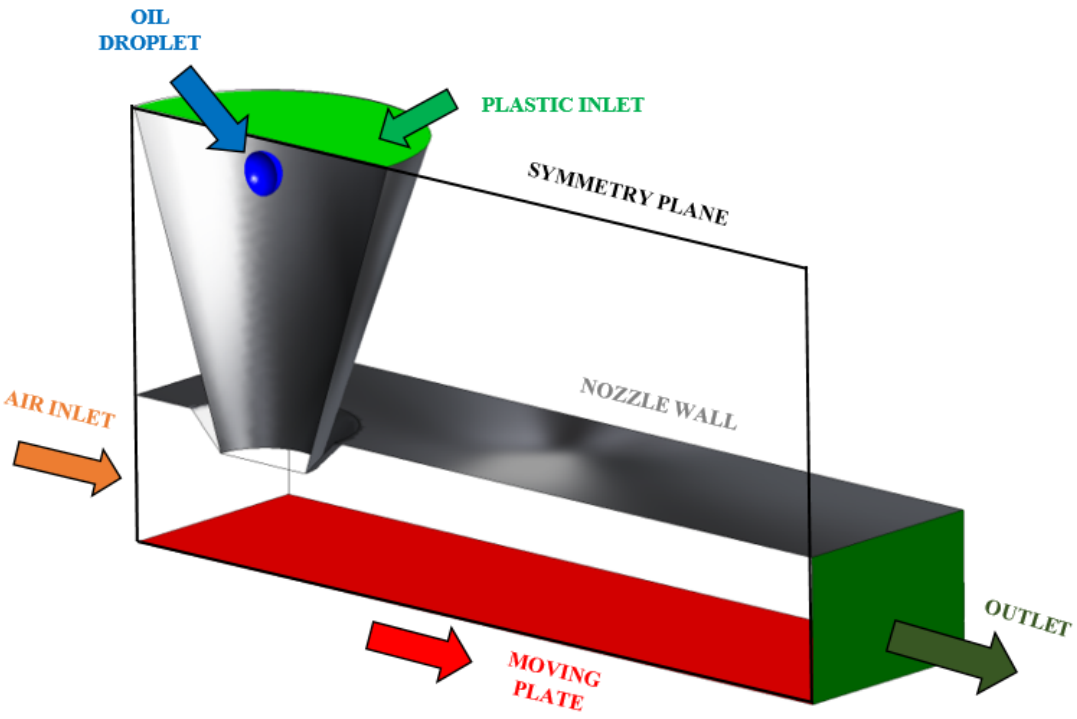

Figure 3.6: Geometry specifying the boundary conditions. The patched oil droplet region is also shown.

(e) The flow is assumed to be laminar. If a cylindrical section of uniform cross-section is considered then we see Poiseuille flow wherein a parabolic profile and a fully developed region is observed. The flow in a fully developed region is dictated by the equation:

$$\frac{v_Z}{\overline{V}} = 2[1 - (\frac{r}{R})^2] for 0 \leq r \leq R \tag{3.10}$$

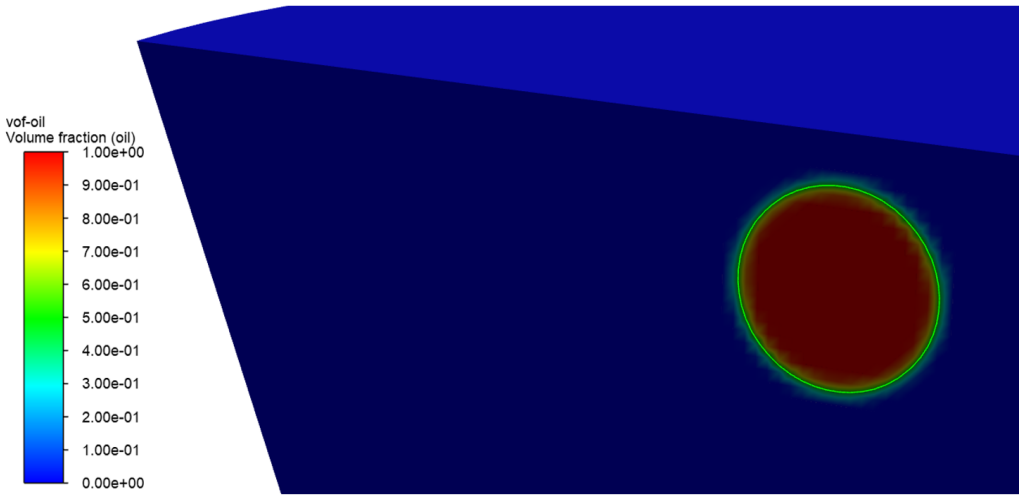

Figure 3.7: A contour representing the volume fraction of oil. The green boundary between the oil and the plastic region represents an iso-surface in a 2D plane.

where v_Z is the axial velocity, $\overline{V}$ is the average velocity inside the nozzle, r is the radial location of the channel and R is the radius of the channel. But in our case, due to the flow directly entering a converging contraction, we do not see a fully developed profile initially.

(f) The interfacial tension between two fluids is a function of temperature. Since temperature effects are neglected, the interfacial tension between the oil droplet and plastic is assumed to be constant throughout the flow.

3.6 Volume Of Fluid (VOF) Model

The Volume of Fluid (VOF) model is widely used to simulate transient flows in a multiphase system where tracking the free surface is of vital importance. VOF is highly robust in tracking the volume fraction of two or more immiscible fluids throughout the domain. VOF is built on the theory that the fluids present in the system do not penetrate each other. A scalar function known as volume fraction

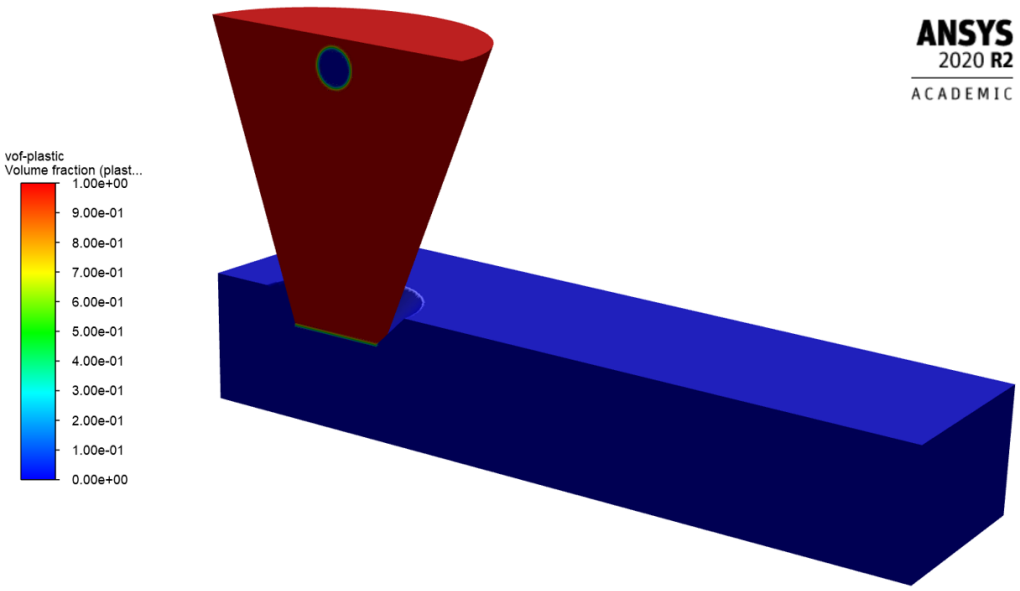

Figure 3.8: A contour of volume fraction of the plastic phase. While the converging contraction is patched with plastic, the cuboidal region is patched with air.

is used to distinguish between the different fluids present in the system. At every discretized element the sum of the volume fractions equal unity. In order words, if we have a fluid 'p' whose volume is patched in a particular cell, there are three situations possible as described in Figure. 3.5. Separation of regions and zones is done in ANSYS for specification of oil, plastic and air volumes. Depending on the phases present those regions and zones are patched with volume fractions of either 1 or 0 as shown in Figures 3.7 and 3.8.

3.7 Boundary Conditions

(a) The velocity of the fluid (V_{inlet}) relative to the boundary is assumed to be zero at the nozzle walls. They are given a no-slip boundary condition.

(b) Utilizing the symmetry condition, one half of the flow domain is analyzed. In

doing so the number of nodes and elements generated decreases which in turn reduces the computational time.

(c) The walls for the air inlet are characterized as moving walls and are given the same velocity as that of the moving substrate (U). V_{inlet} and G is held constant whereas U is varied.

(d) A pressure-outlet boundary condition is specified at the outlet which is open to the atmosphere.

(e) Surface tension effects are captured only between the droplet and the plastic.

	Plastic	**Oil drop**	**Air**
Viscosity ($Pa-s$)	1000	[1, 10, 100, 1000]	1
Density (kg/m^3)	800	970	1

Table 3.4: Material Properties

Parameters	**Values**
Inlet Velocity V_{inlet} (mm/s)	8.33
Velocity of the moving substrate U (mm/s)	[50, 60, 75, 100, 150]
Gap distance between the nozzle tip and moving plate G (mm)	2
Diameter of the nozzle D (mm)	2

Table 3.5: Parameter properties

3.8 Discretization

One of the main factors that dictate the solution accuracy is the quality of the meshing performed. The volume has to be discretized in such a way that the

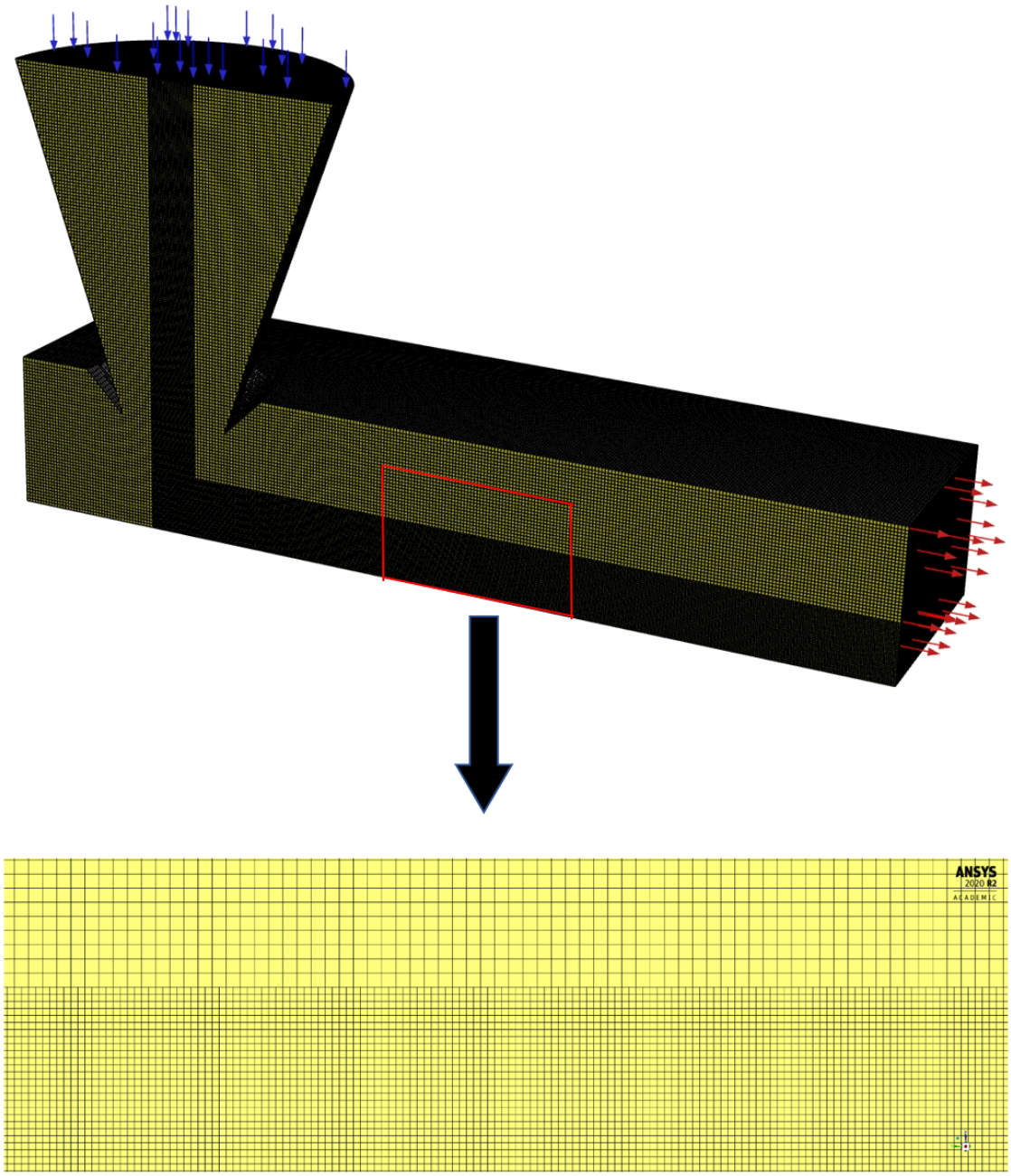

Figure 3.9: Meshing carried out using the Body of Influence method. The zoomed in figure illustrates the difference in the mesh density between the two regions. The flow pathway of the droplet has more than 4X the number of elements compared to the other parts of the channel.

control volumes are small enough to capture the forces at every point in the flow domain. Since the volume of the droplet being considered is of the order of 10^{-4} m, it becomes necessary to choose a grid size that is significantly lesser than that of

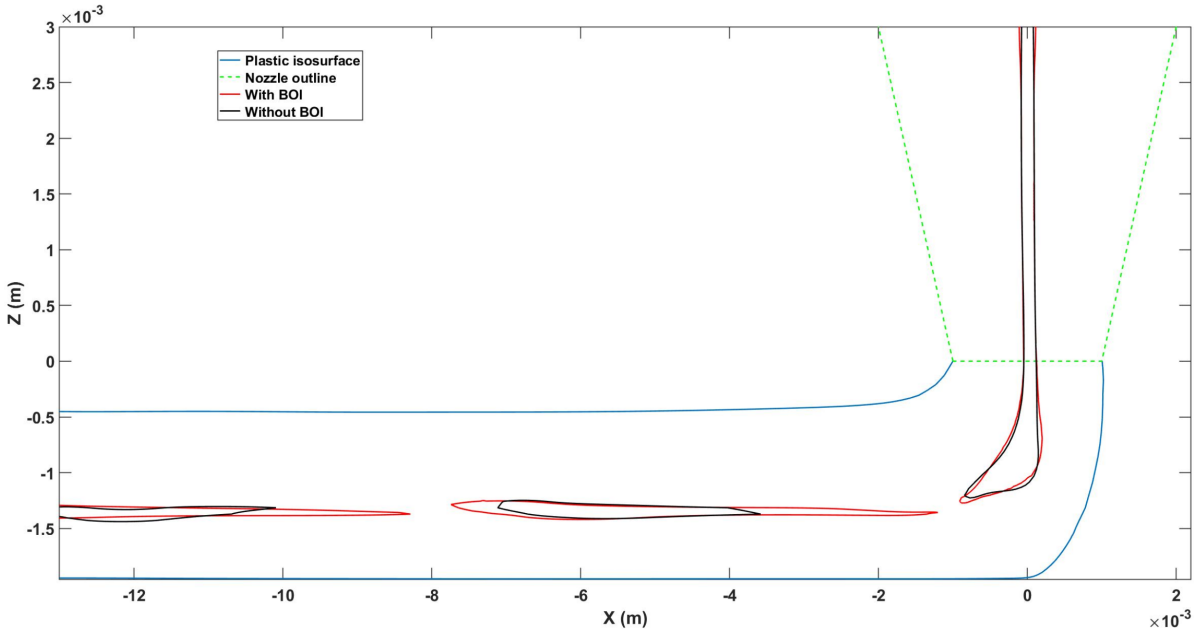

Figure 3.10: Comparison of mass conservation by the two meshing methods adopted.

the droplet in order to get maximum continuity. Cut-Cell technique is used which generates structured hexahedral elements.

CFD is an extremely computationally and time intensive process. Hence, different methods of discretization have to be looked into in order to achieve good computational accuracy with limited time. Since the entire domain is not of primary interest, especially the domain devoid of both oil and plastic, it is not necessary to mesh the body uniformly. Hence, local mesh refinement as seen in Fig. 3.9 is carried out using Body Of Influence (BOI) method, that enables us to perform selective meshing depending on the region of interest.

Grid independence study is performed for three mesh sizes corresponding to coarse, medium and fine densities. Since elongational flow is seen along the center of the channel, strain-rates are monitored in the axial direction of the flow. As seen in Table 3.6, the strain-rates do not vary much with change in mesh sizes. Hence,

forces are said to be stabilized.

Number of nodes	Number of elements	Strain-rate along the centerline (s^{-1})
316,726	294,975	33.768
1,023,863	965,556	32.653
1,994,425	1,942,089	32.4655

Table 3.6: Strain-rate dependence on number of elements

Mass conservation plays an important role in the determination of morphology of the droplet. It was seen that while the coarse mesh gave us a conservation of 83%, with fine mesh we had a conservation of $\approx 98\%$ for $\lambda = 0.001$ and 100% for $\lambda = 1$. Mass loss for $\lambda = 0.001$ is attributed for the formation of extremely thin tails, seen in Fig. 4.15, which the current adopted mesh could not resolve. With respect to the flow of the plastic, it is observed that there is a smooth well-developed boundary between air and plastic for coarser meshes.

Chapter 4: Results and discussion

4.1 Prediction of droplet morphology

A double precision parallel computation is carried out. The Semi-Implicit Method for Pressure Linked Equations (SIMPLE) is used as the scheme. A transient solver with total time specification method is used with a time step interval of δt = 0.007s. The simulations are run until steady state is reached and the oil droplets has completely exited the setup.

4.1.1 Converging Section

Figures. 4.1 and 4.2 illustrate the evolution of droplet morphology with respect to time, along the centerline of the converging nozzle. Since the flow is elongational the evolution vastly differs from that of a drop undergoing rotational flow. At lower time steps we see an initial spherical drop deform into an ellipsoid. The drop attains a long slender shape at which point deformation parameter, neglecting the asymmetric nature can be assumed to tend to ∞. Since, the outer flow (plastic) is sheared extensively and the size of the droplet is very small, viscous forces dominate inside and at the interface of the drop. The Reynold's number for the external flow

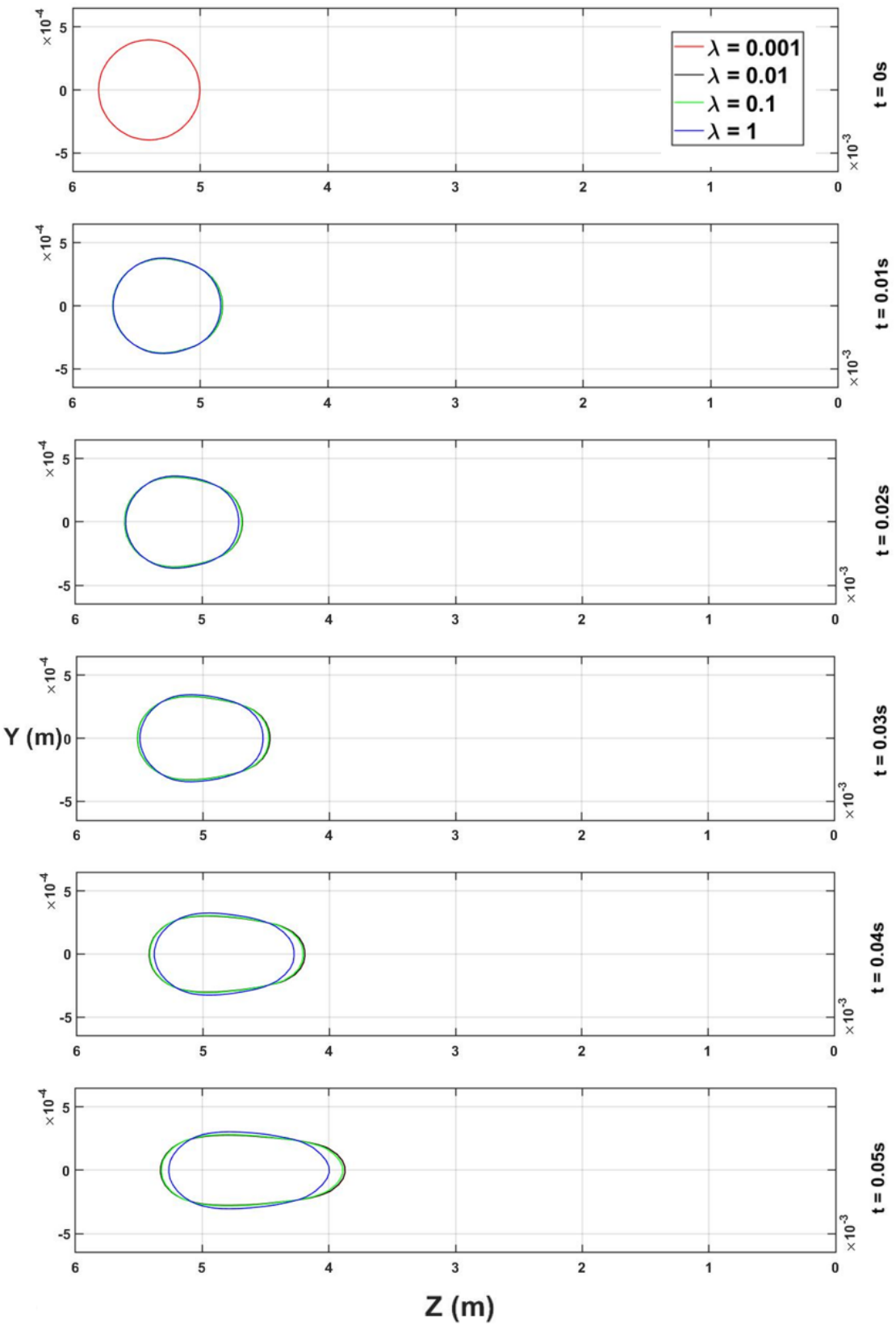

Figure 4.1: 2D Deformation of droplets ($t = 0 \rightarrow 0.05s$) along the center axis in the conical converging section as a function of location. The viscosity ratios are highlighted above.

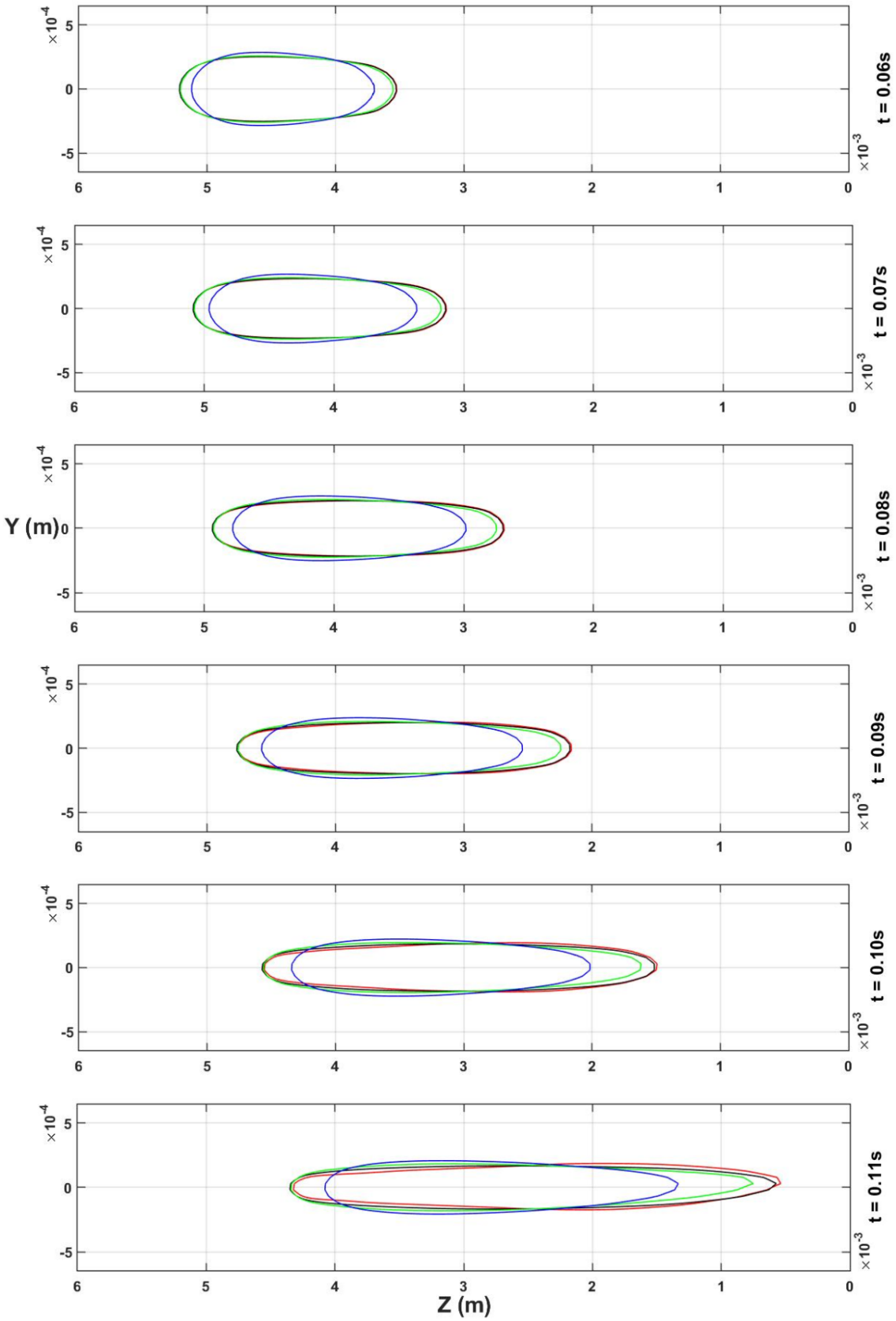

Figure 4.2: 2D Deformation of droplets ($t = 0.06 \rightarrow 0.12s$) along the center axis in the conical converging section as a function of location. The viscosity ratios are highlighted above.

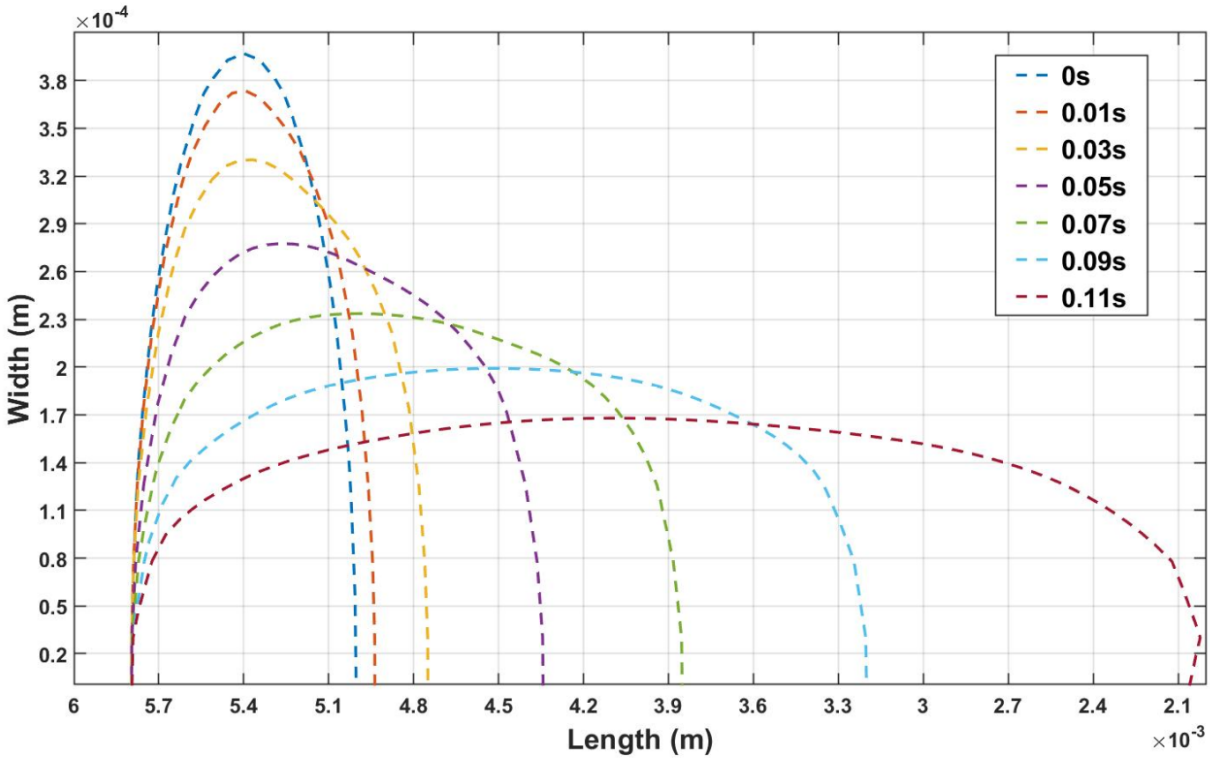

Figure 4.3: Change in width and length of the droplet at various instants for $\lambda = 0.01$

is found to $\approx$ 4 x 10^{-5}, which is in accordance with creeping flows evidenced in highly viscous polymer melts.

We see that during the initial stages the droplet showcases a certain degree of symmetry. As the convergence increases the droplet experiences an inhomogeneous flow and we see an onset of mass transfer ($t = 0.12s$) from the trailing end to the leading end of the droplet. At approximately $t = 0.12s$ for $\lambda = 0.001$ we see that the droplet beginning to change its direction due to the influence of the plastic flow path.

Figures. 4.3 and 4.4 showcase the change in length and width for two viscosity ratios. At $t = 0.12s$ for $\lambda = 1$, the symmetry is evident to an extent, after which in order to aid elongation, the width at both the trailing end and the center decreases.

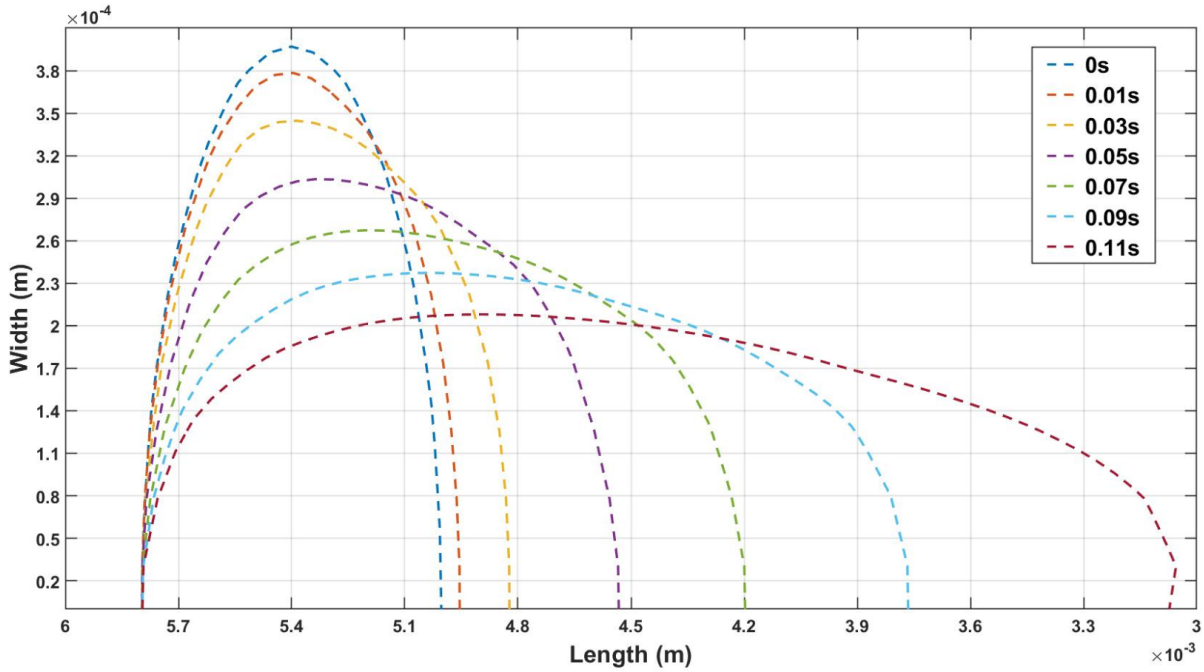

Figure 4.4: Change in width and length of the droplet at various instants for $\lambda = 1$

The deformation for $\lambda = 1$ is seen to be significantly different from that of the three lower ratios. Not only does it withhold a greater degree of symmetry, but it is observed that it stretches significantly lesser. We can conclude that increase in λ, decreases the elongation along the axis in the convergence. The radius of curvature of the droplet decreases on both the ends with increasing rates. But, it is mostly noticeable in the leading end where a pointed end can be observed.

Due to the overall asymmetric nature of deformation at different instants, Taylor's deformation parameter cannot be used. Hence, a dimensionless parameter called Sphericity is used to measure the deviation of the drop from the shape of a sphere. Sphericity is defined as

$$\Psi = \frac{\pi^{1/3}(6V_p)^{2/3}}{A_p} \tag{4.1}$$

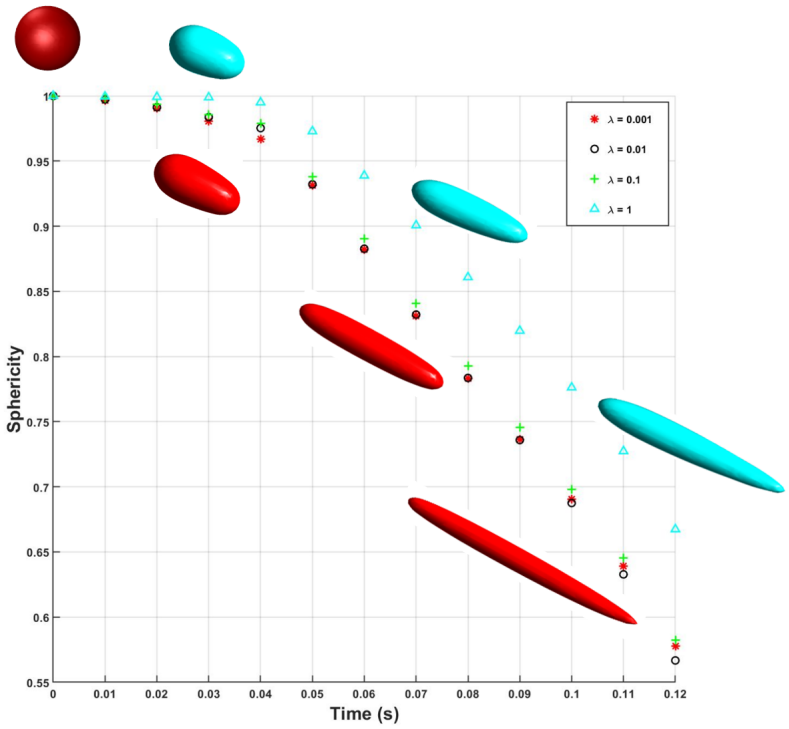

Figure 4.5: Evolution of sphericity of the droplets with time along the plane of symmetry (Drops not illustrated to scale).

where V_p and A_p are the volume and surface area of the droplet respectively. As evident in Figure. 4.5, $\lambda = 1$ retains a greater degree of sphericity, as at higher λ's the rate of elongation of the droplet cannot exceed that of the matrix fluid [37].

In order to explain the different morphologies for the different ratios, the interfacial boundary conditions between the droplet and the plastic have to be considered. Since, the two fluids are incompressible there always exists a moving interface between the droplet and the plastic. Two flow fields, one for plastic and one for droplet can be defined. For $\lambda = 1$, the flow fields of the two fluids perfectly balance each other and the shear stress imposed by them on each other will be equal. In order words the rate of deformation of both the discrete and the matrix phase will be equal.

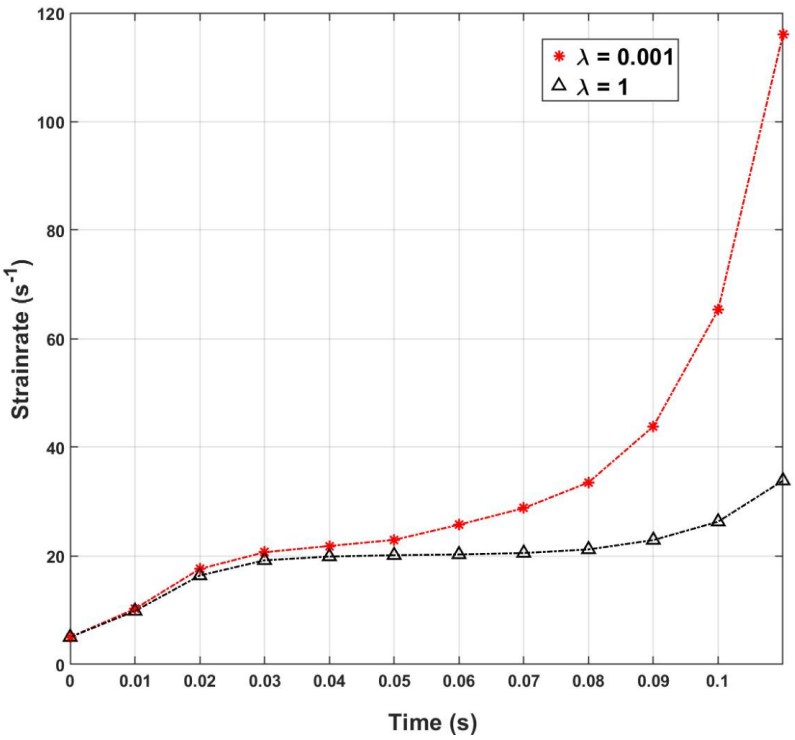

Figure 4.6: Shear-rates at the transient interface between the two phases.

$$\tau_{plastic} = \tau_{oil} \tag{4.2}$$

$$\eta_{plastic} * (\dot{\gamma_{plastic}}) = \eta_{oil} * (\dot{\gamma_{oil}}) \tag{4.3}$$

For a lesser viscous drop, the shear-rate tends to be higher. Hence, the drop stretches more compared to higher viscosities. This is verified by tracking the shear-rates at the interface of the drop and the plastic. For a $\lambda = 1$, there seems to be small increments for every time-step, whereas for $\lambda = 0.001$, the shear-rate increases dramatically. This is in good agreement with the work of Han et al., [38], which conclusively proved that a droplet imposed with a higher shear-rate elongated more than that of a drop with a lower shear-rate. This was also apparent in G. I. Taylor's [28] work that for drops having lower λ's, shear rate required for the drop to burst

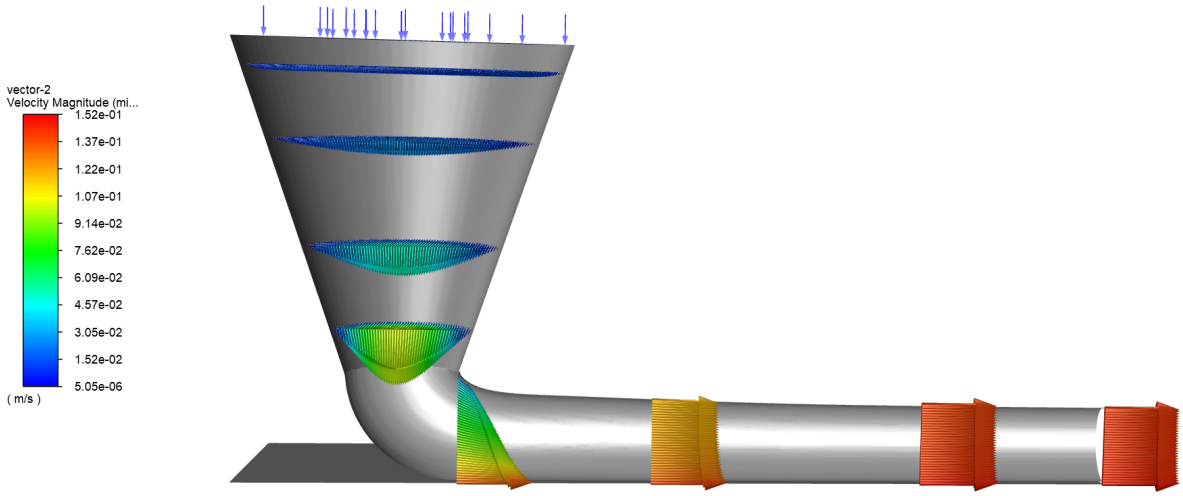

Figure 4.7: Variation of velocity profiles for V/U = 0.5 at different planes during the flow.

into daughter droplets was quite high, which can also be extended to flows having high Capillary numbers.

$$L = (\nabla v)^T = \begin{bmatrix} \frac{\partial v_x}{\partial x} & \frac{\partial v_y}{\partial x} & \frac{\partial v_z}{\partial x} \\ \frac{\partial v_x}{\partial y} & \frac{\partial v_y}{\partial y} & \frac{\partial v_z}{\partial y} \\ \frac{\partial v_x}{\partial z} & \frac{\partial v_y}{\partial z} & \frac{\partial v_z}{\partial z} \end{bmatrix} \tag{4.4}$$

In order to calculate the Capillary numbers associated with the droplet, the extension rates can be extracted along the center-line of the contraction. This is done by determining the total rate of deformation tensor. Rate of deformation tensor in the matrix form is given by Equation. 4.4. All the components of velocity along the centerline of the convergence can be extracted and solved for using the matrix. The Capillary number of the leading end of the drop when it is about to exit the convergence is found to be around 270. As expected, in a multi-flow regime wherein a droplet in suspended in a flow of higher viscosity, the capillary forces are

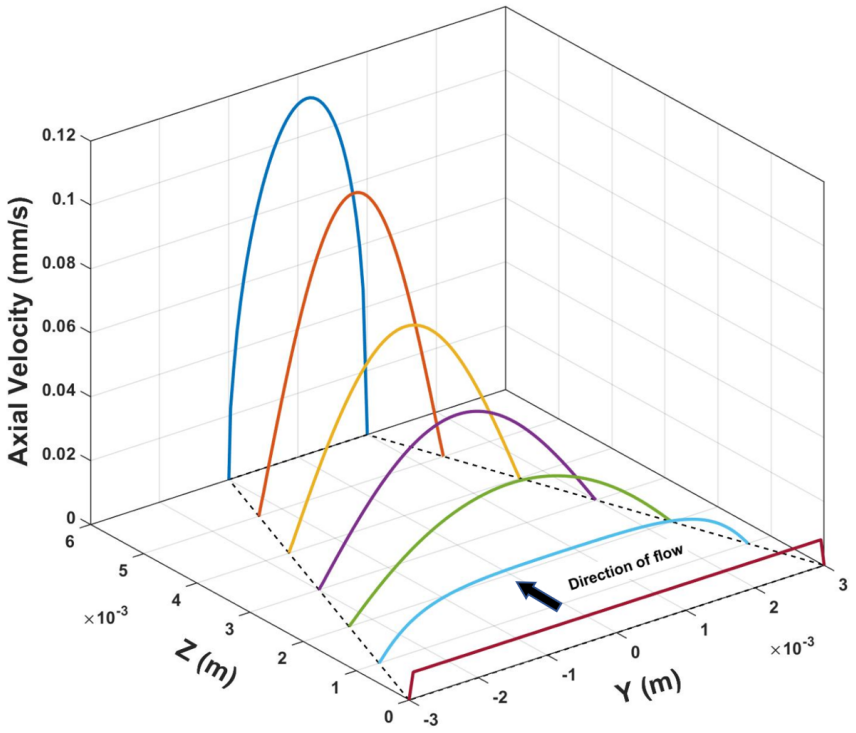

Figure 4.8: Velocity profiles at the various axial positions (0 mm $\geq$ Z $\geq$ 6mm) along the symmetry plane.

negligible compared to the viscous forces and hence we can say that Ca $\rightarrow \infty$.

4.2 Velocity Profiles

As seen in Figure. 4.8, in the converging nozzle, the velocity of the flow is maximum at the center and attains a state of being fully developed as assumed in Equation. 3.5, when the flow is near the nozzle exit. As the fluid accelerates inside the nozzle, the profile gains significant momentum.

'w' component of velocity is dominant along the nozzle whereas 'v' component plays a more dominant role as the plastic gets deposited on the build plate. There is a change and overlap of the two components of velocity in the curvature of the deposited plastic. Due to the change in direction of flow and the movement of the

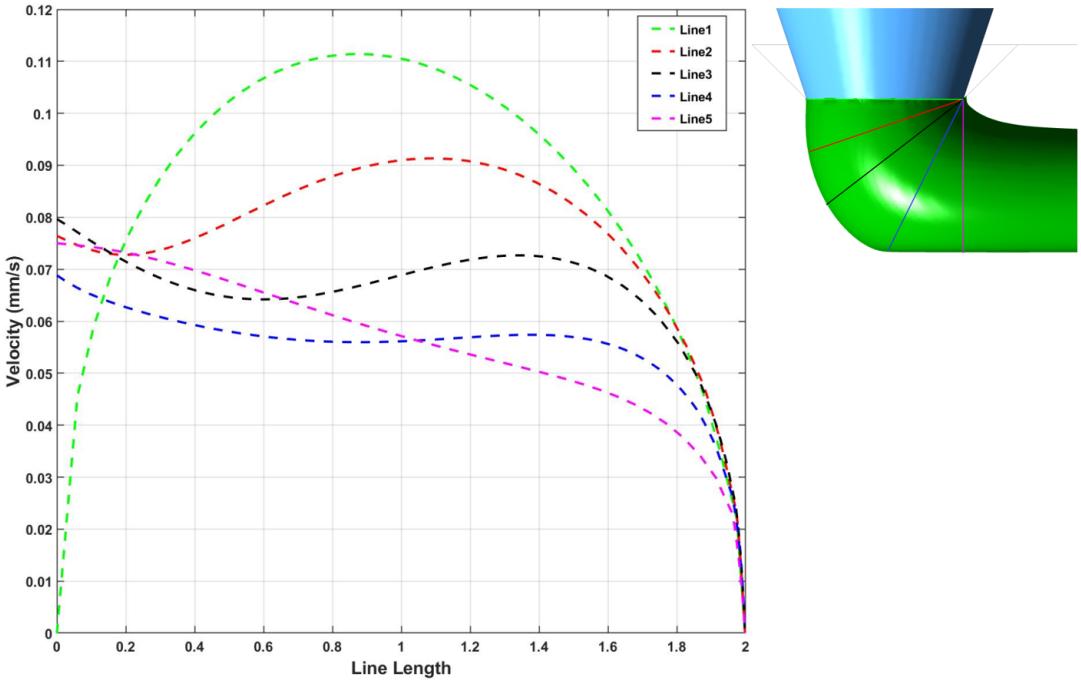

Figure 4.9: Velocity profile development in the curvature section of the deposition for V/U = 1.0

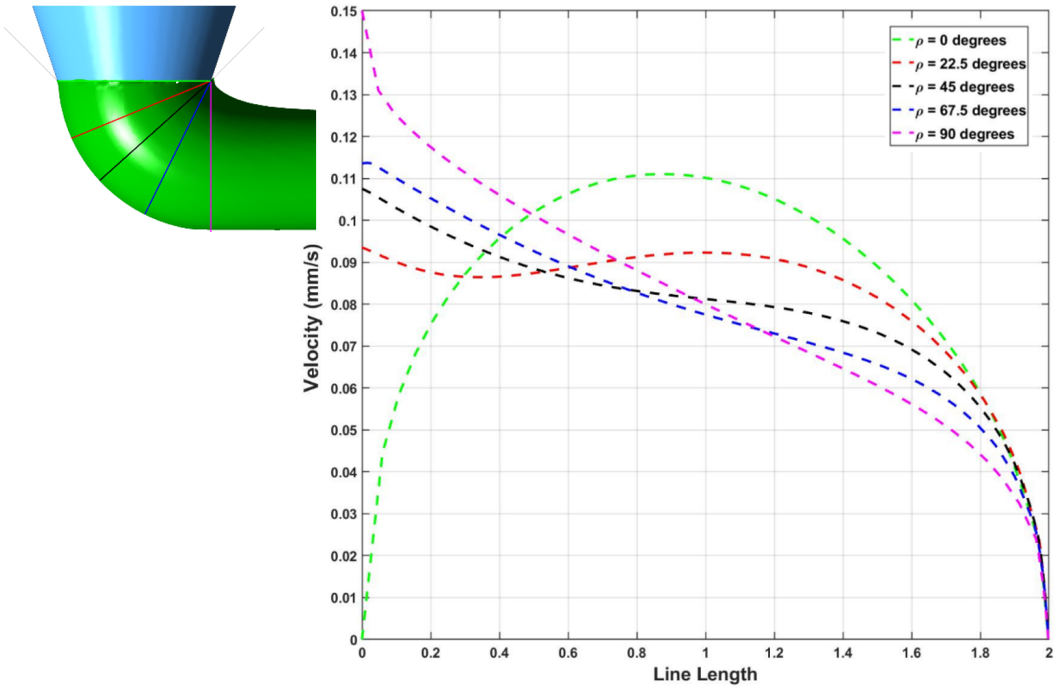

Figure 4.10: Velocity profile development in the curvature section of the deposition for V/U = 0.5

substrate, we see the flow start to deviate from its fully- developed condition. Due to the re-development of velocity profile, the flow profile deviates significantly from a parabola immediately as the plastic starts to exit the nozzle outlet. We see a profile similar to plug flow after the deposition of the plastic.

As seen in Figures. 4.9 and 4.10, the right end of the defined lines have the least velocity as the plastic gets deposited. Once the plastic is deposited, the flow which is in contact with the moving substrate accelerates or decelerates depending on the boundary condition and the flow achieves a steady state after deposition.

4.2.1 Post Convergence

The development of curvature in the exterior flow field extensively dictates the behavior or droplets. As there is a decrease in curvature of the deposited plastic, more mass is accumulated in the leading end the drop becomes narrower with pointed tips. The part of the drop that is still being subjected to extension along the centerline has the least width for lowest λ (longest slender drops). One of the fairly obvious observations is that, lower the viscosity ratio more interesting and complex are the morphologies.

The drops maintain their extended slender shape until the leading end exits the converging nozzle. As mentioned in Section 4.2, depending on the velocity of the build plate, the external flow either accelerates, remains steady or decelerates. When deceleration takes place, the exterior flow field causes the droplet to expand in a direction perpendicular to the flow (radial). This is evident in Figure. 4.11A,

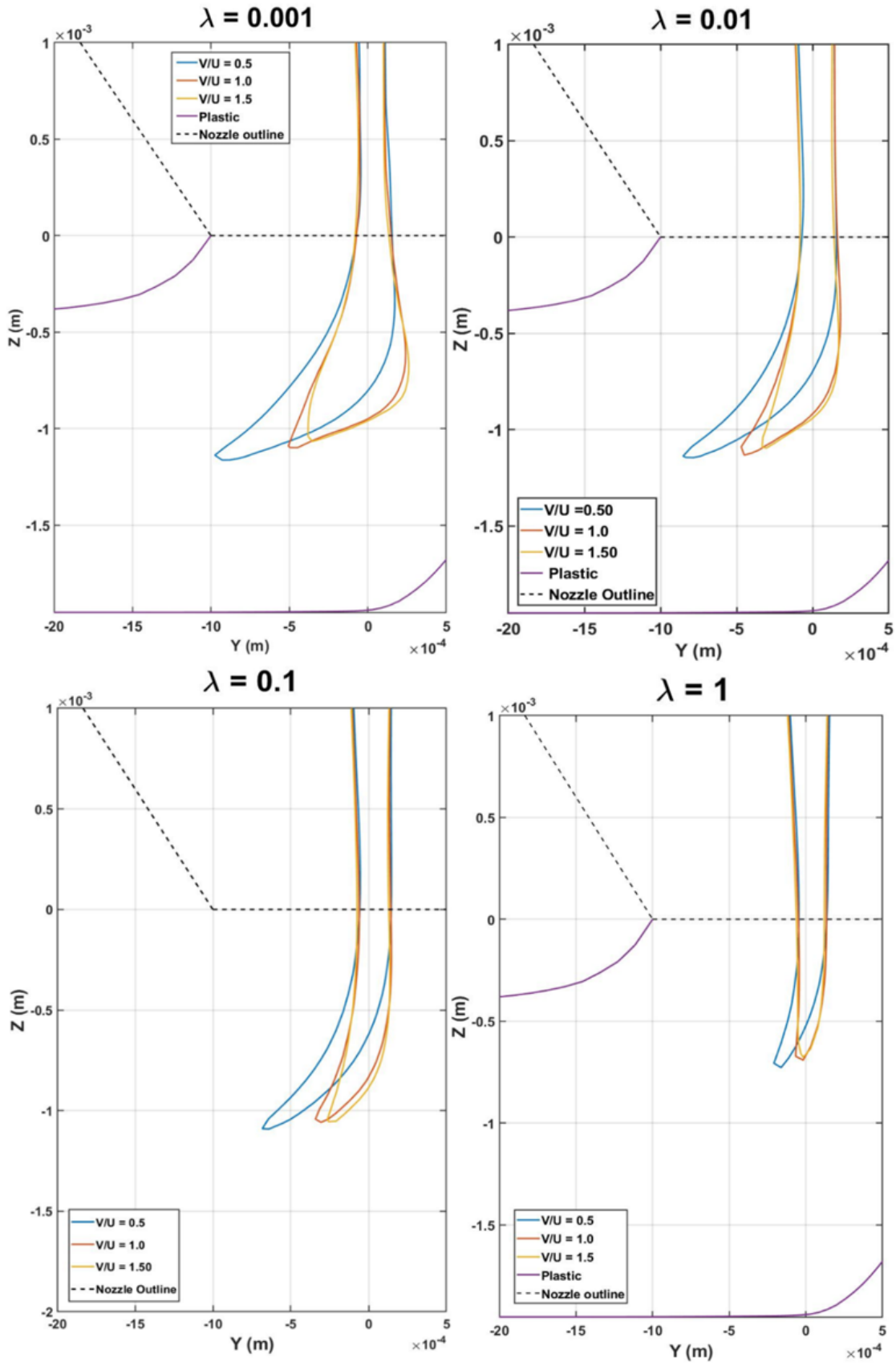

Figure 4.11: 2D Evolution of droplet morphology along the symmetry plane at t = 0.13s. Onset on bulbing for lower ratios is evident.

where for a $\lambda = 0.001$, the weak viscous forces inside the droplet causes the drop to go back to its original steady shape of a sphere when compared to a more viscous drop. This accounts for the onset of 'bulbing' for $\lambda = 0.001$ at $t = 0.13s$.

At this point even though the leading end of the droplet has left the contraction, there exists a fair volume of the droplet in converging section still undergoing extension. Droplets having lower viscosities are susceptible to "bulbing" at the leading end since they experience the most interfacial forces.

For lower V/U ratios it is seen that the droplet elongates more and there is a development of a sharp pointed edge at the leading end of the droplet. As the V/U is decreased, we also see a decrease in the degree of sharpness in the leading tip of the droplet.

As the drops becomes parallel to the external flow-field, the velocity component in the axial direction prevents the drop from going back to the shape of a sphere. These effects are best seen in Figure. 4.15. Lowest viscosity of the drop, owing to its strongest interfacial forces has mass accumulation in the leading end of the droplet. This can be also be attributed to the fact that lower ratios tend to flow more easily without resistance by the external flow field.

Usually, in converging extensional flows the drop attains its maximum elongation at the neck of convergence. But in our case even after the leading end of the droplet exits the contraction, in addition to the continued shear of the polymer on the droplet, there also exists a fair volume of the drop in the converging section still undergoing extension.

While the ends remain pointed for all the cases, the drop continues to stretch

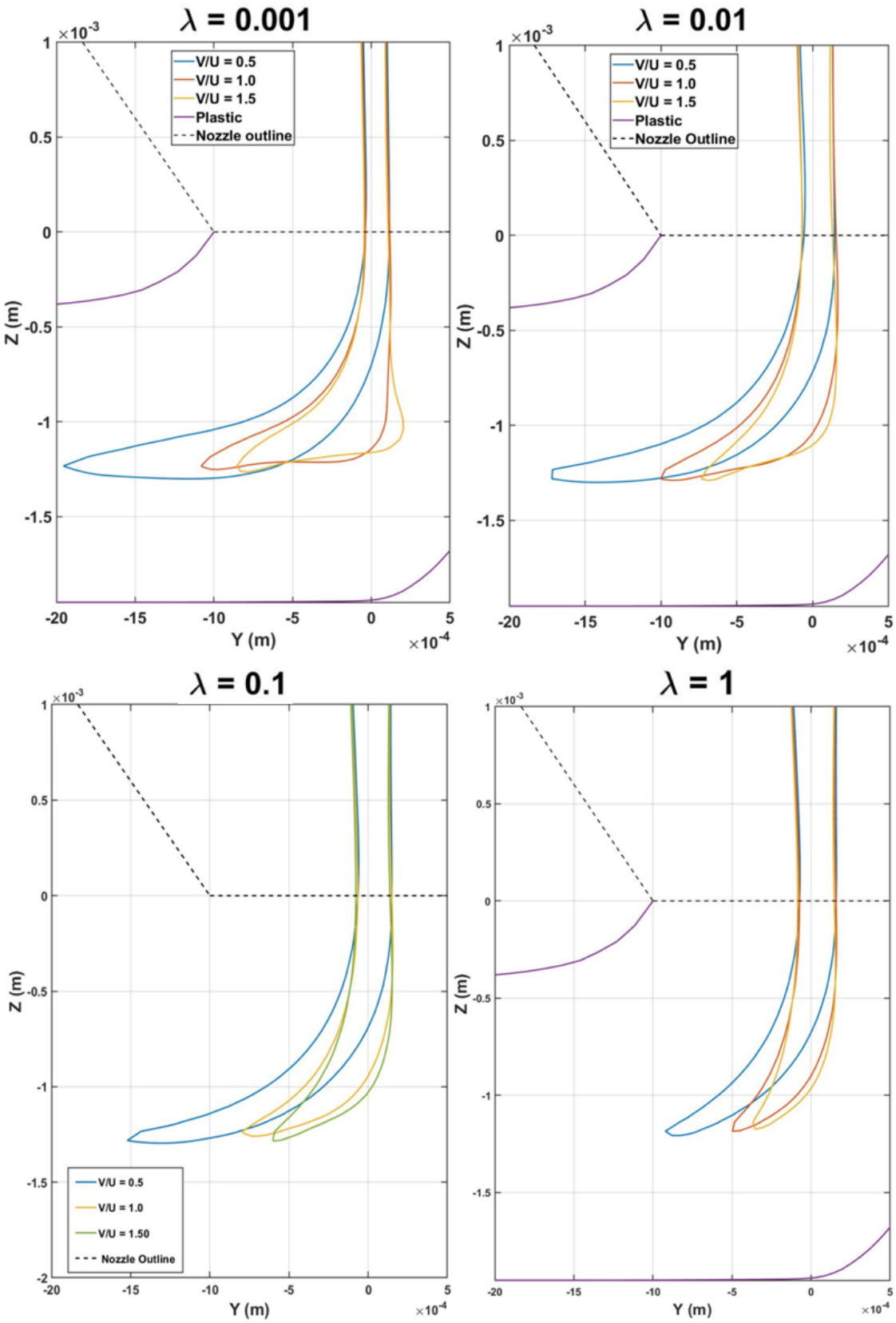

Figure 4.12: 2D Evolution of droplet morphology along the symmetry plane at t = 0.14s.

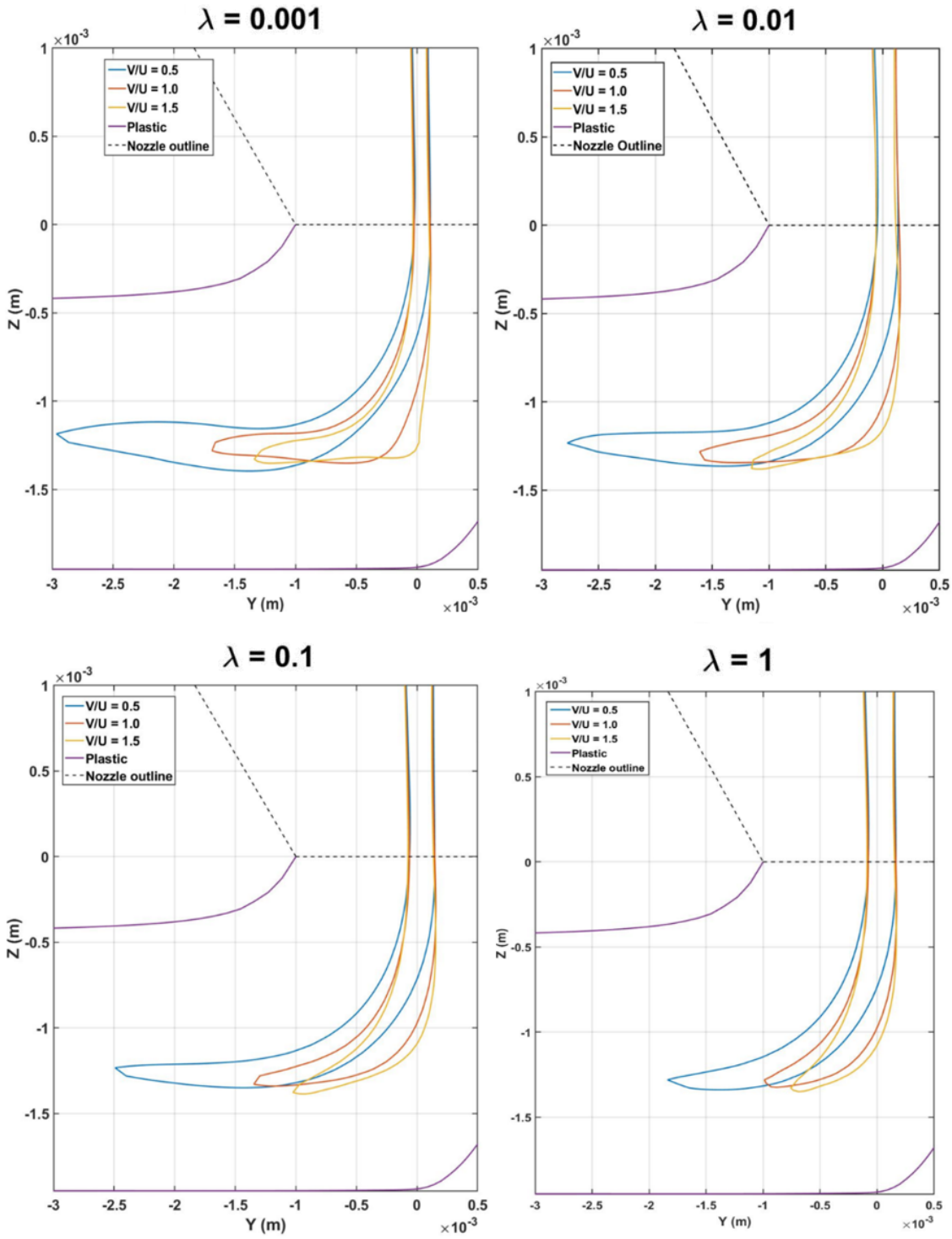

Figure 4.13: 2D Evolution of droplet morphology along the symmetry plane at t = 0.15s.

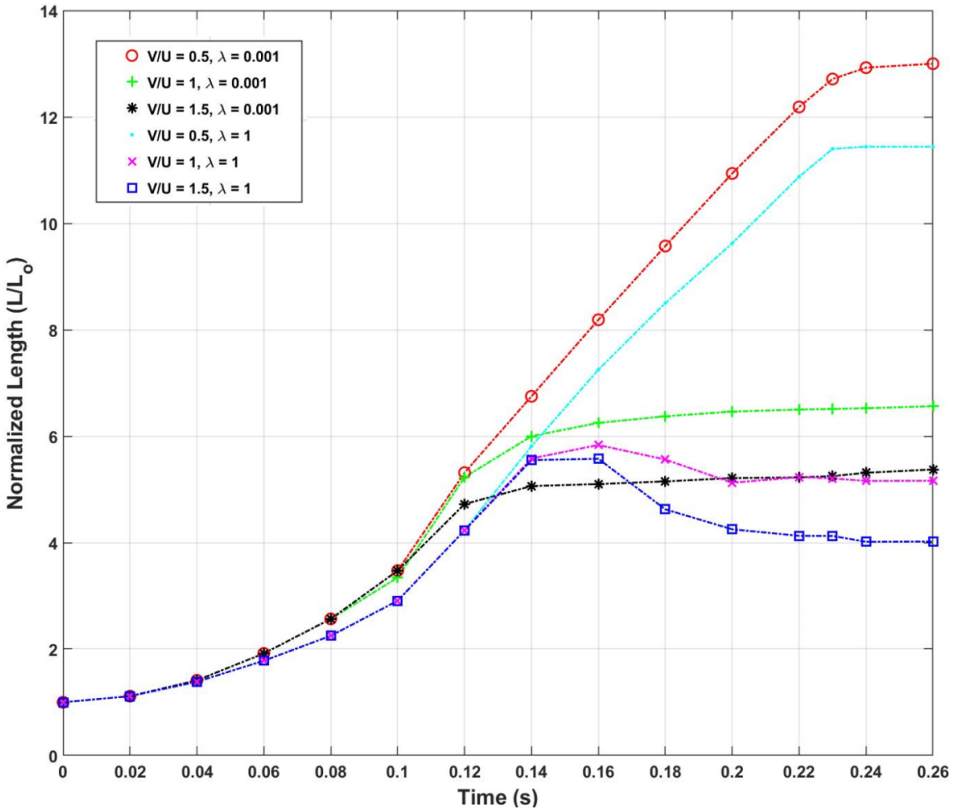

Figure 4.14: Elongation of the droplet for different velocity and viscosity ratios.

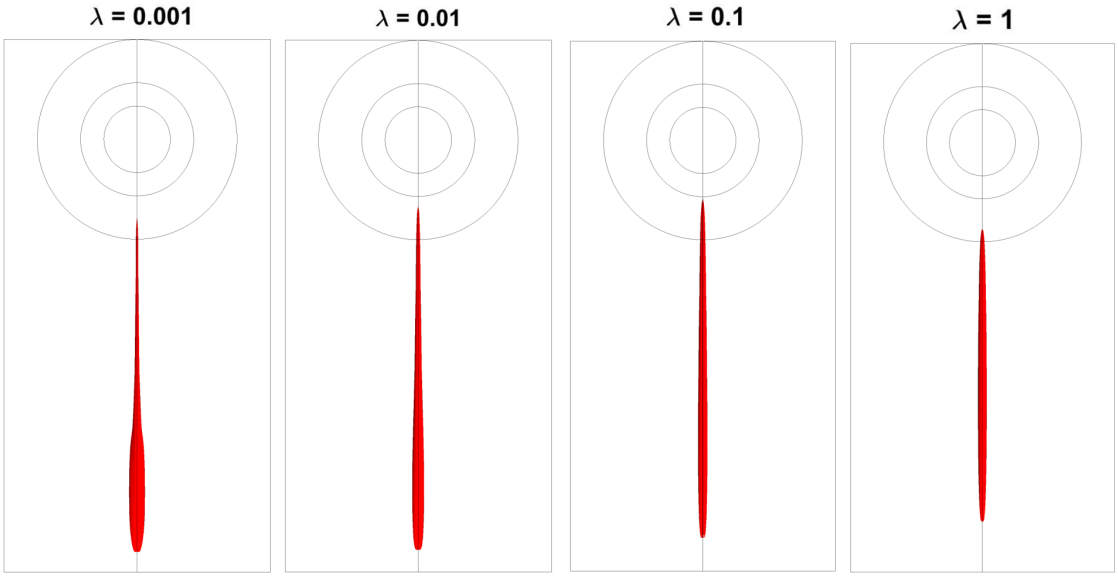

Figure 4.15: Top view of the drops illustrating the different morphologies for a V/U = 0.5

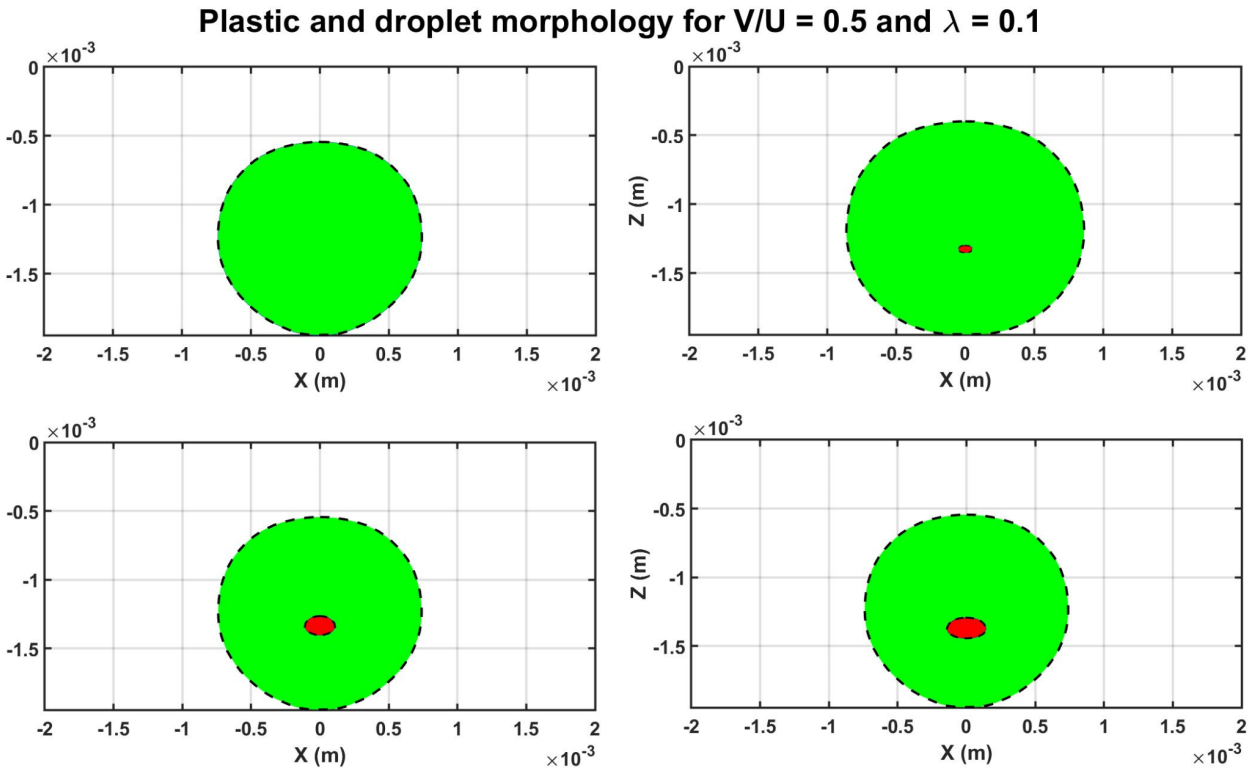

Figure 4.16: Oil and plastic morphologies at different sections of the planes for a ratio of 0.5

with a varying width for different velocity ratios, until it reaches a steady state and is parallel to the exterior flow. It is observed that there is no stretching of the drop once steady state is reached. Figure. 4.14 illustrates the variation of the droplet length for different V/U's and λ 's. It is quite obvious that the lowest V/U and λ stretches the most. The three lower λ's, stretch almost equally, $\lambda = 1$ stretches less due to the balance of shear stress at the interface.

4.3 Prediction of plastic morphology

Once steady state is achieved, reference planes are created at multiple sections in the flow channel in order monitor the morphology of the plastic and oil drop.

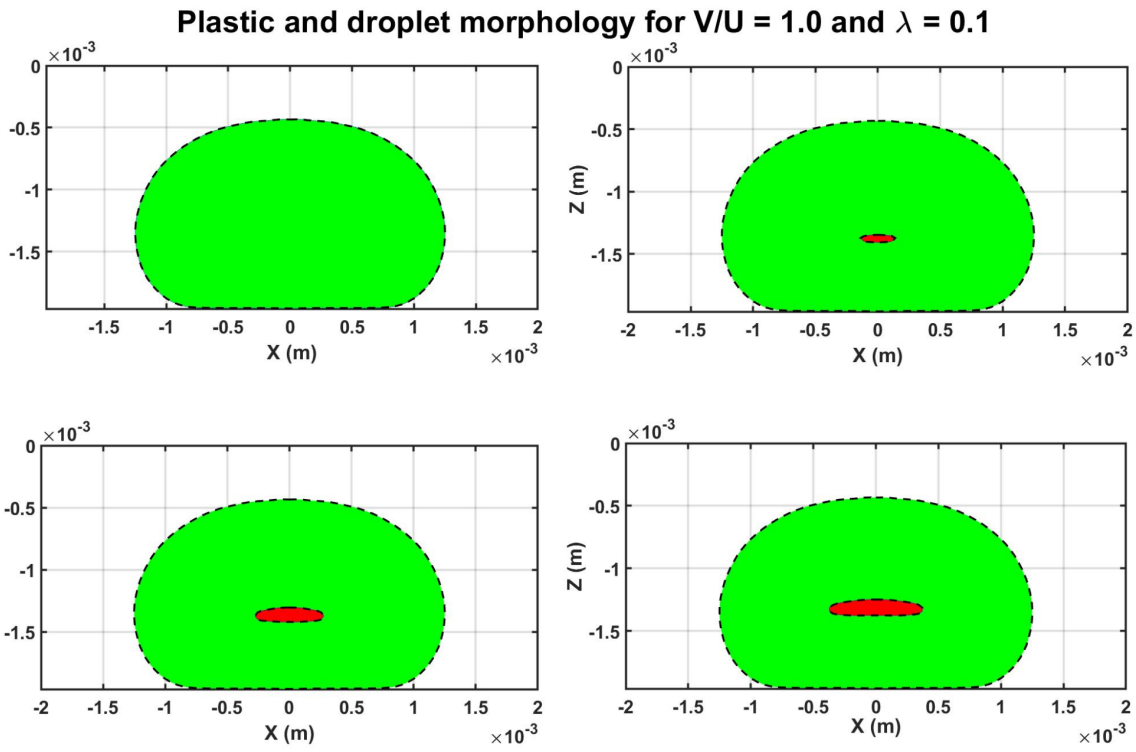

Figure 4.17: Oil and plastic morphologies at different sections of the planes for a ratio of 1

Iso- surfaces which are 3D equivalent of contour lines are created in order to better visualize the morphology. They represent points of equal value (volume fraction, pressure, temperature etc.,) within a controlled volume. These iso-surfaces are created on the reference planes in order to visualize the data and extract the profiles. Datasets are extracted in the form of iso-surfaces into MATLAB where an image processing code is used in order to obtain the area, perimeter and width.

Figures. 4.16 to 4.18 illustrate variation in the morphology of the deposited strands at the outlet for different velocity ratios. The profile is almost circular for a ratio of 0.5, when the plastic is being pulled faster than it is being deposited by the nozzle. It is worth noting that for the lowest ratio seen in Figure. 4.16B, the morphology of plastic is different at the neck of deposition compared to the other

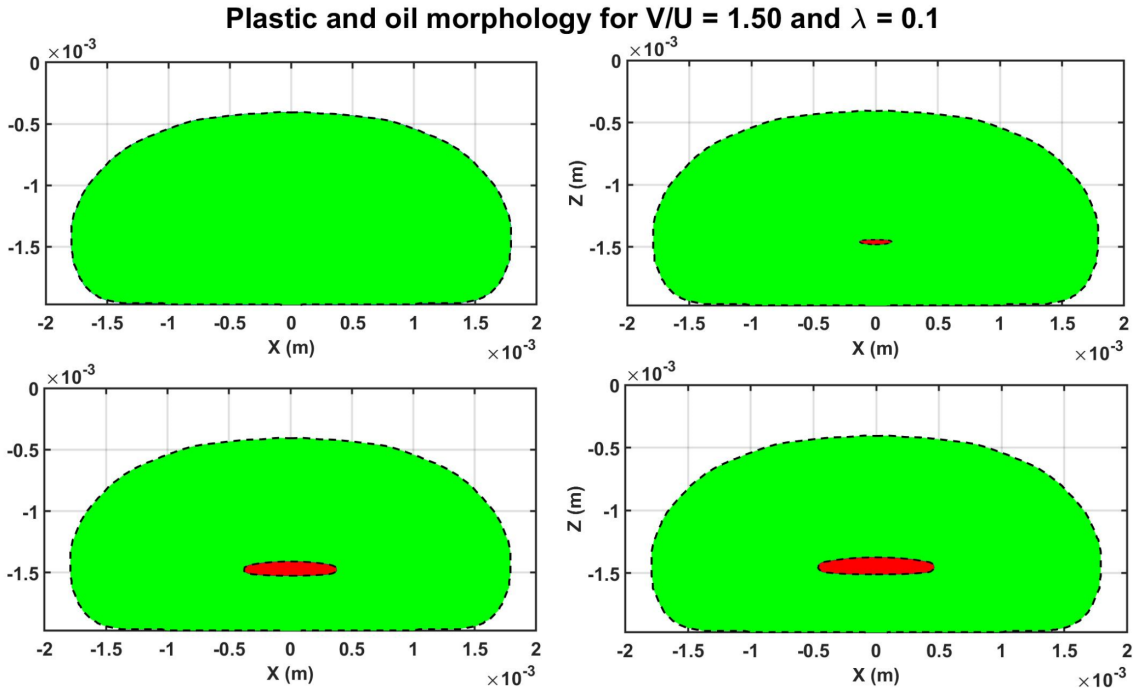

Figure 4.18: Oil and plastic morphologies at different sections of the planes for a ratio of 1.5

locations resulting in uneven areas of the strand across the planes.

As the speed of the build plate is decreased, there is a decrease in curvature of the deposited plastic, as seen in Figures. 4.9 and 4.10. This causes the strand to flatten out for higher velocity ratios. As the velocity ratio is increased, there is a small but noticeable increase in the height of the deposited strand. The upper section of the strand is convex in nature for all the velocity ratios. Gap distances can be changed in order to obtain more flattened, concave shapes.

As first documented by Comminal et al., [64] it is usually assumed that the gap distance (G) is equal to the height of the deposited strand. But it is apparent from the results that that is not the case. For all of these ratios there is an approximately 23-25% decrease in the strand height when compared to the gap distance between the print-head and the substrate.

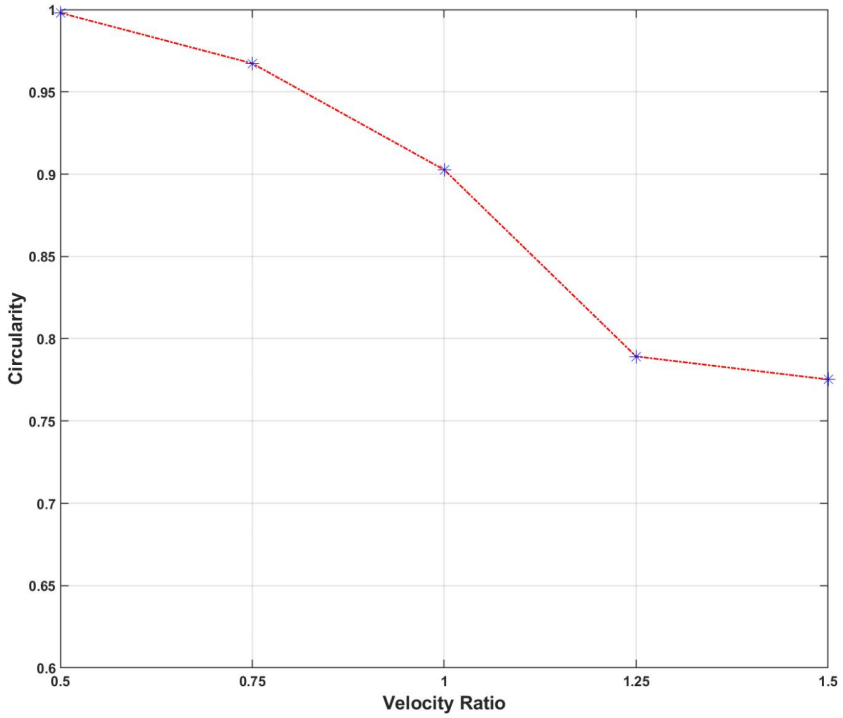

Figure 4.19: Dimensionless circularity for the plastic strands at different ratios.

We can conclude that for a lower print-head speed the plastic spreads more on the build-plate. For most cases the aspect ratio W_{max}/H_{max} taken across multiple planes for a particular velocity ratio remains the same for the plastic, except for the ratio of 0.5.

In order to quantify the compactness of the various morphologies, a dimensioness shape factor called circularity is defined. Circularity is given by

$$C = \frac{4\pi A}{P^2} \tag{4.5}$$

where A and P are the area and perimeter of the cross-section respectively. A circularity of 1 represents a perfect circle and the number decreases as the shape changes.

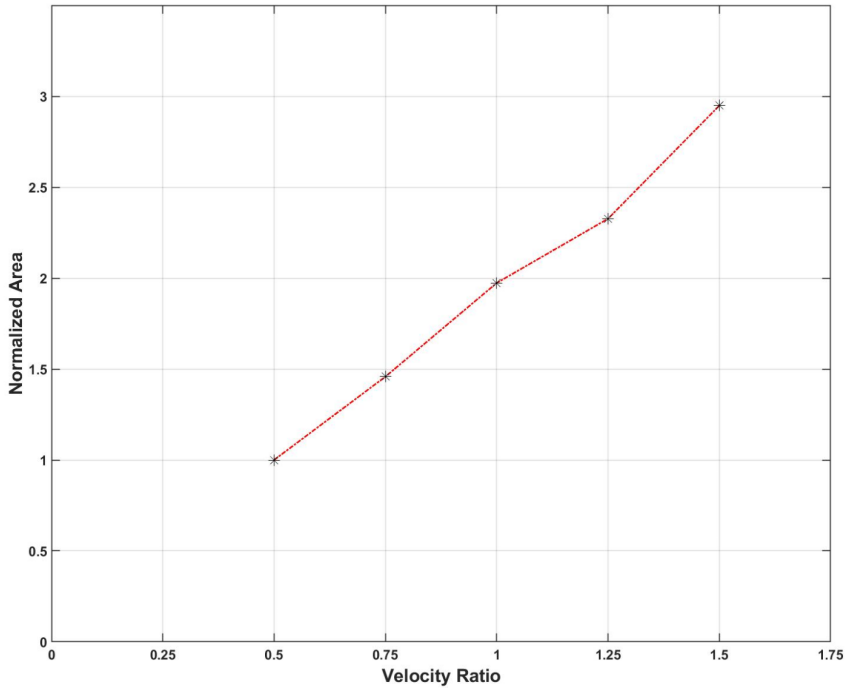

Figure 4.20: Change in area of the deposited strand for different velocity ratios.

It is seen in Figure. 4.19, as the velocity ratio is increased the cross-section of the deposited strand varies from being nearly circular (C = 0.9730), to being oblong for a ratio of 1.5. Even though there is a significant decrease in circularity of the plastic with increasing ratios, as the strand starts to flatten out the circularity becomes more or less equal. As seen in Figure. 4.20, there is a linear increase in area with changing velocity ratios. Changing the gap distance would affect the compactness and areas of the strand adversely and is worth experimenting.

4.4 Summary

A conical nozzle was designed in order to impose a near constant extensional rate on the droplet. Evolution of droplet morphologies are studied for various conditions. Centerline deformation of the droplets were found to be different for each viscosity ratio. Higher degree of deformations is observed for lower λ's when compared with $\lambda = 1$. Due to the polymer matrix, the viscous forces are seen to overflow the interfacial forces. The Capillary numbers are seen to be huge and hence the drop stretches to approximately the same extent regardless of the λ's.

The location of mass concentration of the drop varies as λ is changed. Due to maximum interfacial forces on $\lambda = 0.001$, the occurrence of 'bulbing' is observed. Further simulations demonstrating droplet deformations in different positions (shear) and variations in cross sections of the conical nozzle should be carried out in order to completely understand the behavior of the droplets.

As an antithesis to usual assumptions, the height of the deposited strand is seen to be not equal to the gap distance (G). As the rate of deposition of the plastic strand decreases, more spreading which inturn leads to increase in area of the plastic is observed. Intially spherical, with increase in V/U, the strand slowly achieves a shape of a smooth edged cuboid.

Chapter 5: Conclusion and Future work

The presented work aimed to understand the morphology development of two immiscible fluids. A model mimicking the flow of plastic in a modified converging dye was designed. The nature of center-line droplet deformation inside a viscoelastic polymer undergoing extensional flow was studied. Offset deformations should be simulated in order to understand the effects of shear. Although, difficulty arises when experimentally modelling offset deployments of the drop since controlling and determining the position of injection in these small channels is very cumbersome. A controlled syringe based position determining mechanism capable of injecting constant volumes of the oil drops can be built and offset deployments can be carried out.

Nozzles having different cross-sections can be modelled in order to quantify the variation of the morphology with respect to the cross-section. When performed using a real-life experimental setup, there lies an added disadvantage of not being able to visually inspect the nature of deformation inside the converging section of the nozzle. A imaging system has to be devised that can visualize the changes happening inside the nozzle. Knowledge of the behavior of droplets through contractions help us to control and optimize the process parameters.

The simulation also assumes the model to be iso-thermal which is not the case in real-world extrusion based AM processes. A more complete geometry consisting of a heat-block can be modelled in order to determine the heat transfer effects on the polymer melt. Although, since the whole process takes place in a very short time, not much differences are to be expected. Power law model can also be used in order to quantify the change in viscosity with respect to temperature.

To verify the results obtained from these simulations, an axi-symmetric channel can be machined. However, there are some design considerations to be taken in account while incorporating this into a manufacturing setup. Since polymers have low thermal conductivity (0.13 W/m-K and 0.25 W/m-K for PLA and ABS respectively), there might exists some thermal gradient as the polymer is pushed through the nozzle outlet. In order to account for the increased length and volume of the nozzle, multiple heaters might have to be introduced in order to prevent any temperature gradient between the point of droplet injection and the outlet.

Bibliography

[1] ISO/ASTM. (2013). Additive Manufacturing - General Principles Terminology (ASTM52900) Rapid Manufacturing Association, 10–12.

[2] Horn, T. J., Harrysson, O. L. A. (2012). Overview of current additive manufacturing technologies and selected applications. Science Progress, 95(3), 255–282.

[3] Royal Academy of Engineering. (2013). Additive manufacturing: opportunities and constraints. November 2013, 1–34.

[4] Zeng, W., Guo, Y., Jiang, K., Yu, Z., Liu, Y., Shen, Y., Deng, J., Wang, P. (2013). Laser intensity effect on mechanical properties of wood-plastic composite parts fabricated by selective laser sintering. Journal of Thermoplastic Composite Materials, 26(1), 125–136.

[5] Ning, F., Cong, W., Hu, Y., Wang, H. (2017). Additive manufacturing of carbon fiber-reinforced plastic composites using fused deposition modeling: Effects of process parameters on tensile properties. Journal of Composite Materials, 51(4), 451–462.

[6] Lewis, J. A., Gratson, G. M. (2004). Direct writing in three dimensions. Materials Today, 7(7), 32–39.

[7] Wan, X., Luo, L., Liu, Y., Leng, J. (2020). Direct Ink Writing Based 4D Printing of Materials and Their Applications. Advanced Science, 7(16), 1–29.

[8] Cheng, Y., Chan, K. H., Wang, X. Q., Ding, T., Li, T., Lu, X., Ho, G. W. (2019). Direct-Ink-Write 3D Printing of Hydrogels into Biomimetic Soft Robots. ACS Nano, 13(11), 13176–13184.

[9] Jiang, P., Yan, C., Guo, Y., Zhang, X., Cai, M., Jia, X., Wang, X., Zhou, F. (2019). Direct ink writing with high-strength and swelling-resistant biocompatible physically crosslinked hydrogels. Biomaterials Science, 7(5), 1805–1814.

[10] Nixon, J. R. (2016). Characterization of property structure dependencies for multi-scale polymer composites using extrusion processes, Doctor of Philosophy, University of Maryland, College Park, Maryland, 20740, USA.

[11] Chawla, K. (2012). Composite materials. Springer.

[12] Ramasubramaniam, R., Chen, J., Liu, H. (2003). Homogeneous carbon nanotube/polymer composites for electrical applications. Applied Physics Letters, 83(14), 2928–2930.

[13] Varanasi, P. P., Ryan, M. E., Stroeve, P. (1994). Experimental Study on the Breakup of Model Viscoelastic Drops in Uniform Shear Flow. Industrial and Engineering Chemistry Research, 33(7), 1858–1866.

[14] Rothon, R., Hornsby, P. (2014). Fire Retardant Fillers for Polymers. In Polymer Green Flame Retardants (pp. 289–321). Elsevier Inc.

[15] Gorna, K., Hund, M., Vučak, M., Gröhn, F., Wegner, G. (2008). Amorphous calcium carbonate in form of spherical nanosized particles and its application as fillers for polymers. Materials Science and Engineering A, 477(1–2), 217–225.

[16] Taylor, G. I. (1934). The Formation of Emulsions in Definable Fields of Flow. Proceedings of the Royal Society of London. Series A, Containing Papers of a Mathematical and Physical Character, 146(858), 501–523.

[17] Tomotika, S. (1935). On the instability of a cylindrical thread of a viscous liquid surrounded by another viscous fluid. Proceedings of the Royal Society of London. Series A - Mathematical and Physical Sciences, 150(870), 322–337.

[18] Migler, K. B., Hobbie, E. K., Qiao, F. (1999). In line study of droplet deformation in polymer blends in channel flow. Polymer Engineering and Science, 39(11), 2282–2291.

[19] Mulligan, M. K., Rothstein, J. P. (2011). The effect of confinement-induced shear on drop deformation and breakup in microfluidic extensional flows. Physics of Fluids, 23(2).

[20] Fischer, C., Plummer, C. J. G., Michaud, V., Bourban, P. E., Månson, J. A. E. (2007). Pre- and post-transition behavior of shear-thickening fluids in oscillating shear. Rheologica Acta, 46(8), 1099–1108.

[21] Lubansky, A. S. (2011). Rheology and Its Applications in Biotechnology. In Comprehensive Biotechnology, Second Edition (Vol. 5, pp. 189–201). Elsevier Inc.

[22] Sangli, A., Arispe-Guzman, M., Armstrong, C., Bigio, D. (2019). Experimental studies on liquid additive mixing in a hyperbolic die to incorporate liquids in polymer based additive manufacturing. AIP Conference Proceedings, 2139.

[23] Schmitz, D. P., Ecco, L. G., Dul, S., Pereira, E. C. L., Soares, B. G., Barra, G. M. O., Pegoretti, A. (2018). Electromagnetic interference shielding effectiveness of ABS carbon-based composites manufactured via fused deposition modelling. Materials Today Communications, 15(February), 70–80.

[24] Rahim, T. N. A. T., Abdullah, A. M., Akil, H. M., Mohamad, D., Rajion, Z. A. (2017). The improvement of mechanical and thermal properties of polyamide 12 3D printed parts by fused deposition modelling. Express Polymer Letters, 11(12), 963–982.

[25] DeMeuse, M. T., (2014). High Temperature Polymer Blends. Elsevier.

[26] Khan, I., Mansha, M., Mazumder, M. A. F., Sheardown, H., Al-Ahmed, A., (2019). "Polymer Blends," in Functional Polymers, Springer International Publishing, 513–549.

[27] Takahashi, T., Takimoto, J. I., Koyama, K. (1999). Elongational viscosity for miscible and immiscible polymer blends. II. Blends with a small amount of UHMW polymer. Journal of Applied Polymer Science, 72(7), 961–969.

[28] Taylor, G. I. (1934). The formation of emulsions in definable fields of flow. Proceedings of the Royal Society of London. Series A, Containing Papers of a Mathematical and Physical Character, 146(858), 501–523.

[29] Stone, H. A. (1994).Dynamics of Drop Deformation and Breakup in Viscous Fluids. Annual Review of Fluid Mechanics.

[30] SBentley, B. J., Leal, L. G. (1986). An experimental study of transient effects in the breakup of viscous drops. Journal of Fluid Mechanics, 173, 131–158.

[31] Lee, E. C., Muller, S. J. (1999). Flow light scattering studies of polymer coil conformation in solutions under shear: Effect of solvent quality. Polymer, 40(10), 2501–2510.

[32] Lee, J. S., Dylla-Spears, R., Teclemariam, N. P., Muller, S. J. (2007). Microfluidic four-roll mill for all flow types. Applied Physics Letters,90(7) ,10–13.

[33] Strutt, J. W., Lord Rayleigh. (1979). On the capillary phenomena of jets. Proceedings of the Royal Society of London ,Vol.29 ,71- 97.

[34] Leal, L. G. (1986). An experimental investigation of drop deformation and breakup in steady, two-dimensional linear flows. Journal of Fluid Mechanics, 167, 241–283.

[35] Oliveira, M. S. N., Alves, M. A., Pinho, F. T., McKinley, G. H. (2007). Viscous flow through microfabricated hyperbolic contractions. Experiments in Fluids, 43(2–3), 437–451.

[36] Sangli, A. N. (2017). Experimental Studies on Droplet Deformation in Hyperbolic Converging Channels, Master of Science, University of Maryland, College Park, Maryland, 20740, USA.

[37] Rauwendaal, C. (1991). Mixing in polymer processing. J. Polym. Sci. A Polym. Chem.

[38] Bai Chin, H., Dae Han, C. (1979). Studies on Droplet Deformation and Breakup. I. Droplet Deformation in Extensional Flow. Journal of Rheology, 23(5), 557–590.

[39] Cogswell, F. N. (1978). Converging flow and stretching flow: A compilation. Journal of Non-Newtonian Fluid Mechanics, 4(1–2), 23–38.

[40] F.N. Cogswell,Polym. Engng. Sci., 12 (1972) 62

[41] W.J. Harrison,Proc. Camb. Phil. Sot., 19 (1916) 307.

[42] D.R. Oliver and R. Bragg, Nature (Phys. Sci.), 241 (1973) 131.

[43] L.H. Drexler and C.D. Han, J. Appl. Polym. Sci., 17 (1973) 2369.

[44] Delaby, I., Ernst, B., Froelich, D., Muller, R. (1996). Droplet deformation in immiscible polymer blends during transient uniaxial elongational flow. Polymer Engineering and Science, 36(12), 1627–1635.

[45] Delaby, I., Ernst, B., Germain, Y., Muller, R. (1994). Droplet deformation in polymer blends during uniaxial elongational flow: Influence of viscosity ratio for large capillary numbers. Journal of Rheology, 38(6), 1705–1720.

[46] G. I. Taylor, Proc. R. Soc., A138, 41 (1932)

[47] Tavgac, T. (1972). Drop deformation and breakup in simple shear fields, Doctor of Philosophy, University of Houston.

[48] Migler, K. B. (2000). Droplet vorticity alignment in model polymer blends. Journal of Rheology, 44(2), 277–290.

[49] Gauthier, F., Goldsmith, H.L., Mason, S.G. (1971) Particle motions in non-Newtonian media. Rheologica Acta, 10, 344–364.

[50] Speight, J. (2020). Analysis of oil from tight formations. In Shale Oil and Gas Production Processes (pp. 519–571). Elsevier.

[51] Stalder, A. F., Melchior, T., Müller, M., Sage, D., Blu, T., Unser, M. (2010). Low-bond axisymmetric drop shape analysis for surface tension and contact angle measurements of sessile drops. Colloids and Surfaces A: Physicochemical and Engineering Aspects, 364(1–3), 72–81.

[52] Behroozi, F., Behroozi, P. S. (2018). Reliable determination of contact angle from the height and volume of sessile drops. ArXiv, 28.

[53] Quincke, G. H. (1870), "Ueber Capillaritats-Erscheinungen an der gemeinschaftlichen Oberflche von Flssigkeiten," Ann. Phys. Chem. 139, 1–89.

[54] Behroozi, F. (2012). Determination of contact angle from the maximum height of enlarged drops on solid surfaces. American Journal of Physics, 80(4), 284–288.

[55] Broseta, D, and Ragil, K. Parachors in terms of critical temperature, critical pressure and acentric factor. United States: N. p., 1995. Web.

[56] Van Krevelen, D. W., Te Nijenhuis, K. (2009). Acoustic Properties. In Properties of Polymers (pp. 505–522). Elsevier.

[57] Avinc, O., Khoddami, A. (2010). Overview of Poly(lactic acid) (PLA) fibre: Part II: Wet Processing; Pretreatment, Dyeing, Clearing, Finishing, and Washing Properties of Poly(lactic acid) Fibres. Fibre Chemistry, 42(1), 68–78.

[58] Mehrabi Mazidi, M., Edalat, A., Berahman, R., Hosseini, F. S. (2018). Highly-Toughened Polylactide- (PLA-) Based Ternary Blends with Significantly Enhanced Glass Transition and Melt Strength: Tailoring the Interfacial Interactions, Phase Morphology, and Performance. Macromolecules, 51(11), 4298–4314.

[59] Valerio, O., Misra, M., Mohanty, A. K. (2018). Statistical design of sustainable thermoplastic blends of poly(glycerol succinate-co-maleate) (PGSMA), poly(lactic acid) (PLA) and poly(butylene succinate) (PBS). Polymer Testing, 65(December), 420–428.

[60] Briassoulis, D., Giannoulis, A. (2018). Evaluation of the functionality of bio-based food packaging films. Polymer Testing, 69(May), 39–51.

[61] Van Krevelen, D. W., Te Nijenhuis, K. (2009). Interfacial Energy Properties. In Properties of Polymers (pp. 229–244). Elsevier.

[62] van Oss, C. J., Chaudhury, M. K., Good, R. J. (1988). Interfacial Lifshitz—van der Waals and Polar Interactions in Macroscopic Systems. Chemical Reviews, 88(6), 927–941.

[63] Good, R. J., Girifalco, L. A. (1957). A Theory for the Estimation of Surface and Interfacial Energies. I. Derivation and Application to Interfacial Tension. J. Phys. Chem., 24(13), 561–565.

[64] Comminal, R., Serdeczny, M. P., Pedersen, D. B., Spangenberg, J. (2018). Numerical modeling of the strand deposition flow in extrusion-based additive manufacturing. Additive Manufacturing, 20, 68–76.

[65] Sun, S., Zhang, T. (2020). Review of classical reservoir simulation. In Reservoir Simulations (pp. 23–86). Elsevier.